

# The viewing angle in AGN SED models, a data-driven analysis

Andrés F. Ramos Padilla<sup>1,2\*</sup>, Lingyu Wang<sup>1,2</sup>, Katarzyna Małek<sup>3,4</sup>, Andreas Efstathiou<sup>5</sup>  
and Guang Yang (杨光)<sup>6,7</sup>

<sup>1</sup>Kapteyn Astronomical Institute, University of Groningen, Landleven 12, 9747 AD Groningen, The Netherlands

<sup>2</sup>SRON Netherlands Institute for Space Research, Landleven 12, 9747 AD Groningen, The Netherlands

<sup>3</sup>National Centre for Nuclear Research, Pasteura 7, 02-093 Warsaw, Poland

<sup>4</sup>Aix Marseille Univ. CNRS, CNES, LAM, Marseille, France

<sup>5</sup>School of Sciences, European University Cyprus, Diogenes Street, Engomi, 1516 Nicosia, Cyprus

<sup>6</sup>Department of Physics and Astronomy, Texas A&M University, College Station, TX 77843-4242, USA

<sup>7</sup>George P. and Cynthia Woods Mitchell Institute for Fundamental Physics and Astronomy, Texas A&M University, College Station, TX 77843-4242, USA

Accepted XXX. Received YYY; in original form ZZZ

## ABSTRACT

The validity of the unified active galactic nuclei (AGN) model has been challenged in the last decade, especially when different types of AGNs are considered to only differ in the viewing angle to the torus. We aim to assess the importance of the viewing angle in classifying different types of Seyfert galaxies in spectral energy distribution (SED) modelling. We retrieve photometric data from publicly available astronomical databases: CDS and NED, to model SEDs with X-CIGALE in a sample of 13 173 Seyfert galaxies located at redshift range from  $z = 0$  to  $z = 3.5$ , with a median redshift of  $z \approx 0.2$ . We assess whether the estimated viewing angle from the SED models reflects different Seyfert classifications. Two AGN models with either a smooth or clumpy torus structure are adopted in this paper. We find that the viewing angle in Type-1 AGNs is better constrained than in Type-2 AGNs. Limiting the viewing angles representing these two types of AGNs do not affect the physical parameter estimates such as star-formation rate (SFR) or AGN fractional contribution ( $f_{\text{AGN}}$ ). In addition, the viewing angle is not the most discriminating physical parameter to differentiate Seyfert types. We suggest that the observed and intrinsic AGN disc luminosity can: i) be used in  $z < 0.5$  studies to distinguish between Type-1 and Type-2 AGNs, and ii) explain the probable evolutionary path between these AGN types. Finally, we propose the use of X-CIGALE for AGN galaxy classification tasks. All data from the 13 173 SED fits are available at Zenodo<sup>†</sup>.

**Key words:** methods: data analysis, statistical – astronomical data bases: miscellaneous – Techniques: photometric – galaxies: Seyfert

## 1 INTRODUCTION

The presence of an optically thick structure in a Seyfert galaxy (Antonucci & Miller 1985) led to the creation of the unified model of active galactic nuclei (AGN), where an obscuring torus explains the variety of AGN types due to the orientation with respect to the line of sight (e.g. Antonucci 1993; Urry & Padovani 1995). This simple model uses the viewing angle to separate AGN galaxies into two types: unobscured (Type-1 AGN) and obscured (Type-2 AGN). Type-1 AGNs have broad emission lines, in terms of the full width at half maximum (FWHM), while Type 2 AGNs do not, due to differences in the viewing angle  $i$ . We observe narrow-line regions (NLR, with  $\text{FWHM} \lesssim 1000 \text{ km s}^{-1}$ ) or broad line regions (BLR, with  $\text{FWHM} \gtrsim 1000 \text{ km s}^{-1}$ ) depending on  $i$ . In Type-1 AGN, the BLR and NLR are viewed directly because the galaxies are viewed at small angles with respect to the line of sight ( $i \approx 0 - 30^\circ$ ), while for Type-2 AGN, only the NLR is visible because the galaxies are viewed at high angles with respect to the line of sight ( $i \approx 70 - 90^\circ$ )

and obscuration hides the BLR (e.g. Antonucci 1993; Kauffmann et al. 2003). However, in the last decade, the “zoo” of AGNs has become more complex and difficult to explain with this simple toroidal structure model (Padovani et al. 2017) and the viewing angle has not been easy to estimate (e.g. Marin 2016). Besides, obscuration is not static and may depend on different physical conditions that may vary (e.g. Hönic & Kishimoto 2017; Hickox & Alexander 2018). In addition, the “changing look” AGNs cannot be explained with the unified model, but rather with the accretion state of the AGN (LaMassa et al. 2015; Elitzur et al. 2014). Therefore, updates to the unified model of AGNs have been proposed describing new AGN scenarios such as clumpy structures (e.g. Krolik & Begelman 1988; Nenkova et al. 2002; Dullemond & van Bemmel 2005), radiation-pressure modes (e.g. Fabian et al. 2008; Ricci et al. 2017; Wada 2015), polar dust (e.g. Braatz et al. 1993; Cameron et al. 1993; Efstathiou et al. 1995; Efstathiou 2006) and disc winds (e.g. Emmering et al. 1992; Netzer 2015; Elitzur & Shlosman 2006; Hönic 2019).

The study of Seyfert galaxies can help to understand the nature of the AGNs in these scenarios. Seyferts are moderate luminosity AGN galaxies that possess high excitation emission lines (Padovani et al. 2017) which can be used to classify these galaxies in Type-1 AGN

\* ramos@astro.rug.nl (AFRP)

† <https://doi.org/10.5281/zenodo.5221764>

(Seyfert 1, hereafter Sy1) and Type-2 AGN (Seyfert 2, hereafter Sy2) in catalogues (e.g. Véron-Cetty & Véron 2010). In addition, Seyfert sub-classes, like the narrow line Sy1 (NLSy1, Osterbrock & Pogge 1985; Rakshit et al. 2017) or the intermediate Seyfert types (Osterbrock 1981; Winkler 1992), could be ideal to understand the new AGN scenarios (Elitzur et al. 2014). Nevertheless, large samples of spectroscopically classified Seyfert galaxies are mainly limited to  $z < 1$  (e.g. Véron-Cetty & Véron 2010; Koss et al. 2017).

One solution to increase the number of Seyfert galaxies at higher redshifts is to identify AGNs through colour selections in IR broad-bands (a compilation of these selection criteria is presented by Padovani et al. 2017, table 2) and then observe their spectrum in optical wavelengths for the classifications. However, these photometric broad-bands can also be used in spectral energy distribution (SED) analysis, which allows us to obtain a more reliable estimation of the contribution of the AGN than using only the IR colours (Ciesla et al. 2015; Dietrich et al. 2018; Ramos Padilla et al. 2020; Mountrichas et al. 2021; Poulisis et al. 2020). The contribution of the AGN in SED models comes from AGN templates (e.g. Mullaney et al. 2011; Bernhard et al. 2021) or AGN models (e.g. Pier & Krolik 1992; Granato & Danese 1994; Efstathiou & Rowan-Robinson 1995; Fritz et al. 2006; Nenkova et al. 2008; Stalevski et al. 2012, 2016; Siebenmorgen et al. 2015; Tanimoto et al. 2019), which are fitted together with dust emissions and stellar populations (e.g. Calistro Rivera et al. 2016; Leja et al. 2018; Boquien et al. 2019) in different configurations (check Thorne et al. 2021; Pérez-Torres et al. 2021, for an overview of the most popular SED fitting codes). SED models without an AGN contribution do not provide the adequate physical properties of AGNs (e.g. Leja et al. 2018; Dietrich et al. 2018), which could lead to over-estimations in star-formation rate (SFR) and stellar masses, especially in X-ray selected AGNs (Florez et al. 2020).

When the AGN is included in the SED modelling, it is shown to be possible to identify Type-1 and Type-2 AGN (e.g. Calistro Rivera et al. 2016; Ramos Padilla et al. 2020). These AGN types tend to show differences not only in the spectrum, but also in colours from photometric bands. For example, Type-1 AGNs tend to have typically bluer colours than Type-2 because of their higher brightness and lower extinction in the UV and optical bands (Padovani et al. 2017). In addition, in Type-1 the contribution from the AGN seem to be more dominant in UV and NIR–MIR bands, while for Type-2 this contribution is dominant in MIR–FIR bands (Ciesla et al. 2015), which can explain why it is possible to differentiate Type-1 and Type-2 AGNs according to their fractional contribution of the AGN to the IR (Fritz et al. 2006). Therefore it should also be possible to identify Sy1 and Sy2 galaxies with SED analysis when observing broad-band emissions.

In this work, we aim to assess the importance of the estimated viewing angle in classifying AGN galaxies, and highlight its implications in high-redshift studies. Particularly, we gather a sample of Seyfert galaxies with available photometry in astronomical databases to develop a data-driven approach with easily accessible data. We use X-CIGALE (Yang et al. 2020), a modified version of CIGALE (Boquien et al. 2019), one of the most popular SED tools to obtain physical parameters in host galaxies and AGN itself. X-CIGALE has several AGN-related improvements compared to CIGALE, ideal for this work. In addition, we test the two different AGN models inside X-CIGALE to see how the classifications depend on the selected model. We compare two popular machine learning techniques, random forest (Breiman 2001) and gradient boosting (Chen & Guestrin 2016), with individual physical parameters when classifying unclassified and discrepant cases.

We present the Seyfert sample selection, the description of the SED

models and the verification of the estimations with a similar model in Sect. 2. Then, we select our main physical parameters, compare the estimated galaxy physical parameters from different AGN SED setups, and we compare different classifications in Sect. 3. After that, we present the discussions about the role of the viewing angle, its implications and possible bias of these results (Sect. 4). Finally, we present our conclusions (Sect. 5).

## 2 DATA AND ANALYSIS

### 2.1 Seyfert Sample

Seyfert galaxies are a good starting point to differentiate between Type-1 and Type-2 AGN, as described by the AGN unification model. Thus, we selected a sample of Seyfert galaxies by combining the *SIMBAD* astronomical database (Wenger et al. 2000, hereafter **SMB**)<sup>1</sup> and the dedicated catalogue of AGNs by Véron-Cetty & Véron (2010, hereafter **VCV**). **SMB** is widely used for retrieving basic information of galaxies in an homogeneous manner, while **VCV** is one of the most popular catalogues for AGN studies. From **SMB**, we picked galaxies whose main type was Seyfert, including: Seyfert 1 (Sy1), Seyfert 2 (Sy2) and, unclassified Seyfert galaxies. From **VCV**, we selected all Seyfert types galaxies, including all intermediate numerical classifications (e.g. Sy1.5). We cross-matched **SMB** and **VCV** samples using a cross-matching radius of  $2''$ . We removed galaxies where the difference in redshifts between the catalogues ( $|\Delta z|$ ) was higher than 0.01, which is the limit of the reported numerical accuracy between the catalogues, as shown in Figure 1. This decision help us to avoid misidentification and uncertain redshifts in the sample of Seyfert galaxies.

#### 2.1.1 Classification type

We used the classification type from both **SMB** and **VCV** samples. Classifications types in **VCV** come from spectroscopic measurements with SDSS data (Abazajian et al. 2009), while classification types in **SMB** are a compendium of the literature. The information gathered in *SIMBAD* was manually added by documentalist till the 90's, and now is done semi-automatically with *COSIM* (Brunet et al. 2018). Unfortunately, the source of the classifications was not recorded until 2006, therefore almost half of the Seyfert classifications in **SMB** are marked as coming from *SIMBAD*. A small fraction of our Seyfert galaxies ( $\sim 5\%$ ) still have an unknown source, as the object type classification is still under development (Oberto et al. 2020)<sup>2</sup>. Therefore, classifications in **SMB** should be taken with caution. If the classification source is unknown and the main Seyfert classification in **SMB** matches **VCV**, we assume that the classification source is **VCV**. If the main Seyfert classification source is unknown and the classification in **VCV** is Seyfert 3 (also known as LINERs) we remove the galaxies from the sample. We re-classified the remaining unknown sources, 49 galaxies, as unclassified Seyfert to study them further. These decisions led us to a sample of 18 921 Seyfert galaxies.

For the classifications in **SMB**, we found: i) Almost half of the classifications (45%) came from the basic data of the galaxy (assigned by the astronomical database); ii) Toba et al. (2014) work contributed to 21% of the Sy1 and Sy2 classifications iii) Zhou et al. (2006), Oh et al. (2015), and Rakshit et al. (2017) together contributed to 25% of

<sup>1</sup> Data and classification types of the galaxies were retrieved on 2020 December 3.

<sup>2</sup> We use the 2018 August 2 classification version.

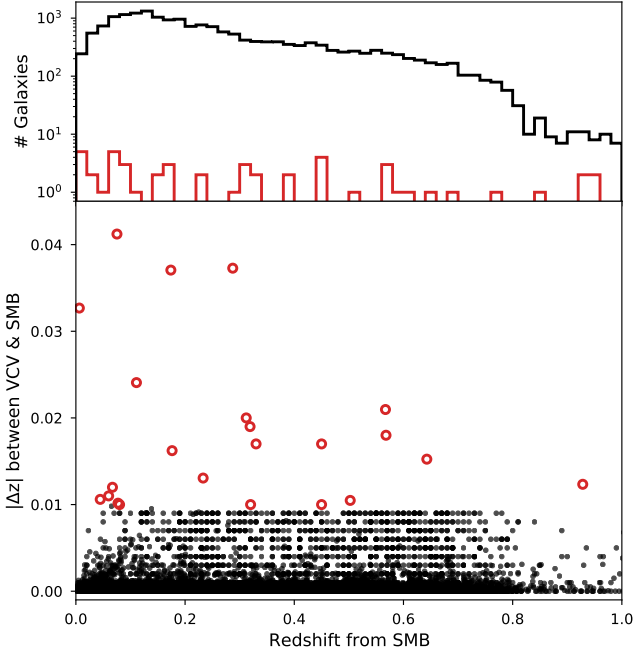


**Figure 1.** Redshift distribution for the matches between **SMB** and **VCV** catalogues. *Upper-panel:* Histogram of the redshift distribution for galaxies where the difference in redshift between the catalogues was below (black line) or above (red line) the threshold at 0.01. Only a few galaxies were discarded using this threshold. *Bottom-panel:* Absolute difference in redshift ( $|\Delta z|$ ) between the catalogues with respect to the **SMB** redshift. Galaxies with redshifts above 1, or with a large difference in redshift in the catalogues are not shown. Discarded galaxies are indicated as red circles.

**SMB** classifications, all of them in Sy1 galaxies. The **SMB** sample contains in total: 13 760 Sy1, 5 040 Sy2, and 121 unclassified Seyfert galaxies.

In **VCV**, we found 17 different Seyfert type classifications. In this work, we focus on the typical Sy1, Sy2 and unclassified Seyferts which all together account for 71% of the sample. We added the narrow-line Sy1 (NLSy1) galaxies (e.g. Zhou et al. 2006; Rakshit et al. 2017) to the Sy1 classification because most of the NLSy1 galaxies in **VCV** are classified as Sy1 in **SMB**. However, some differences in the estimates may indicate that the total accretion power in NLSy1 galaxies is higher than in normal Sy1 galaxies, as we verified in Appendix A. Three of the NLSy1 galaxies (2MASX J10194946+3322041, 2MASS J09455439+4238399 and 2MASX J23383708-0028105) were classified as Sy2 in **SMB**, so we reclassified them as unclassified Seyfert for further study. In addition, we checked the subgroups between Sy1 and Sy2 as divided by Osterbrock (1977, 1981) and Winkler (1992) which account for 5% of the sample. We denoted a small fraction of the galaxies from **VCV** ( $\sim 1\%$ ), which do not fall in the classifications described before (e.g. LINERS, NLSy1.2 and polarised classifications), as alternative Seyfert galaxies. **VCV** sample contains in total: 13 180 Sy1, 4 567 Sy2, 84 unclassified Seyfert galaxies, 920 in the intermediate numerical subgroups between Sy1 and Sy2, and 170 alternative Seyfert galaxies.

### 2.1.2 Photometry

We used 31 bands in the UV-FIR wavelength range to get a well-sampled SED for our sample of Seyfert galaxies. We list the selected bands for the SED modelling in Table 1 with their respective effective wavelength and number of galaxies detected in that band. We retrieved photometric values of these bands available in CDS<sup>3</sup> and NED<sup>4</sup>. CDS and NED photometric data points are ideal for this data-driven work as they are published and curated by other researchers, saving time in the photometric reduction. However, we needed to make sure that the retrieved data were good enough for our purpose.

We keep in mind that the use of heterogeneous measurements may lead to some systematics in the analysis. For example, for galaxies in the local Universe, or where the instrument resolution is good enough to resolve the galaxies, measurements will come from specific regions within the galaxies, like their centres. In contrast, for galaxies at higher redshifts or instruments where the resolution is not high enough to resolve them spatially the measurements will correspond to the whole galaxy as we observe the galaxies as unresolved point sources. Fortunately, in terms of spatial resolution, most of the galaxies in this sample could be treated as point sources for most of the instruments operating at different wavelengths, therefore we expect measurements at different wavelengths to be consistent with each other. When this is not the case, discrepant apertures at different wavelengths will lead to unphysical jumps in the SED models, which will give us erroneous fittings that we can ignore before going further with the analysis.

Hence, we followed a series of steps to obtain a set of galaxies with useful photometry. First, we decided not to use upper or lower limits from published values in CDS or NED. Second, we remove duplicate data photometry values between the CDS and NED, keeping the value reported in CDS. Third, we used the mean value when more than one measurement was available per band. These measurements can also come from the same apertures but from different works or methods. Fourth, we selected photometric data points with a relative error (after propagating the initial reported errors) below 1/3. Finally, we accounted for the absolute calibration error for each band as in Ramos Padilla et al. (2020), where instrument-dependent uncertainties were added to the measurement uncertainties.

We constrained the galaxies to have good coverage over the optical and IR wavelengths. We only include sources satisfying both criteria: i) more than five photometric data points in wavelengths between  $0.1 - 3\mu\text{m}$  (*GALEX*, *SDSS* and *2MASS*), and ii) more than three photometric data points in wavelengths between  $3 - 500\mu\text{m}$  (*Spitzer*, *WISE*, *IRAS* and *Herschel*). With these criteria, we ended up with 13 173 Seyfert galaxies for which we carry out the following SED modelling analysis.

We also looked for X-ray and radio photometric data points. However, the coverage at those wavelengths was not homogeneously tabulated in CDS or NED as in the selected bands in Table 1. We decided not to use X-ray and radio wavelengths as this will require more computational and time efforts for a few number of galaxies (only  $\sim 0.01\%$  of the sample). In addition, currently X-CIGALE does not include a AGN radio component. We discuss the implications of not using X-ray data in Sect. 4.5.

<sup>3</sup> <http://cdsportal.u-strasbg.fr/>

<sup>4</sup> The NASA/IPAC Extragalactic Database (NED) is funded by the National Aeronautics and Space Administration and operated by the California Institute of Technology.

**Table 1.** Photometric bands used in the SEDs modelling. The last column shows the number of galaxies detected in a given band.

Mission or Survey	Band	Effective Wavelength [ $\mu\text{m}$ ]	Number of galaxies
GALEX	FUV	0.152	6456
	NUV	0.227	9266
SDSS	u	0.354	12024
	g	0.477	12542
	r	0.623	12326
	i	0.762	12274
	z	0.913	11604
2MASS	J	1.25	7018
	H	1.65	6566
	Ks	2.17	8215
Spitzer	IRAC-1	3.6	4063
	IRAC-2	4.5	4048
	IRAC-3	5.8	458
	IRAC-4	8.0	447
	MIPS1	24.0	809
	MIPS2	70.0	225
WISE	MIPS3	160.0	110
	W1	3.4	13170
	W2	4.6	13165
	W3	12.0	12361
IRAS	W4	22.0	8295
	IRAS-1	12.0	462
	IRAS-2	25.0	634
	IRAS-3	60.0	979
	IRAS-4	100.0	722
Herschel	PACS-blue	70.0	265
	PACS-green	100.0	178
	PACS-red	160.0	303
	SPIRE-PSW	250.0	840
	SPIRE-PMW	350.0	476
	SPIRE-PLW	500.0	233

## 2.2 SED Models

### 2.2.1 Parameter grids

We modelled the SEDs of the Seyfert galaxies with X-CIGALE (Yang et al. 2020). X-CIGALE is a modified version of CIGALE (Boquien et al. 2019), a SED fitting code based on an energy balance principle. The difference between X-CIGALE and CIGALE is the addition of i) an X-ray photometry module and, ii) a polar dust model in AGNs. These two enhancements help to connect the X-ray emission to the UV-to-IR SED, and account for dust extinction in the polar angles, respectively. The X-ray emission is helpful to constrain AGN intrinsic accretion power in the SED (Lyu & Rieke 2018; Toba et al. 2021), and the polar dust follow observational results from MIR interferometry (López-Gonzaga et al. 2016; Ramos Almeida & Ricci 2017).

We included six modules which account different galactic emission processes to fit the SEDs. The first module defines the star-formation history (SFH). We used a delayed SFH model for our sample of galaxies because this has shown a good agreement in different types of galaxies with ongoing or recent starburst events (Dietrich et al. 2018; Ramos Padilla et al. 2020), and can provide better estimates for physical parameters such as star-formation rate (SFR) and stellar mass (Ciesla et al. 2015). The second module defines the single-age stellar population (SSP). We selected the standard Bruzual & Charlot (2003) model taking into account the initial mass function (IMF) from Chabrier (2003) and a metallicity close to solar. The dust attenuation law from Calzetti et al. (2000) is our third module.

This module helps us control the UV attenuation with the colour excess  $E(B-V)$ , and also the power-law slope ( $\delta$ ) that modifies the attenuation curve. The fourth module takes the dust emission in the SED into account. We modelled the dust emission following Dale et al. (2014), implementing a modified blackbody spectrum with a power-law distribution of dust mass at each temperature,

$$dM \propto U^{-\alpha} dU, \quad (1)$$

where  $U$  is the local heating intensity. We also included the nebular emission module although we did not change the default parameters.

The sixth and most important module for this work is the module that describes the AGN SED. For our experiments setups, we selected the two AGN modules available in X-CIGALE: A simple smooth torus (Fritz et al. 2006), and a tho-phase (smooth and clumpy) torus (Stalevski et al. 2016, also known as SKIRTOR). For both models, we covered a larger sample of parameters for the viewing angle  $i$  and the fraction of AGN contribution to the IR luminosity  $f_{\text{AGN}}$  (Ciesla et al. 2015, eq. 1),

$$L_{\text{IR}}^{\text{AGN}} = f_{\text{AGN}} \times L_{\text{IR}}^{\text{total}}, \quad (2)$$

to investigate the effect of  $i$  in Seyfert galaxies. In addition, we set the extinction law of polar dust to the SMC values (Prevot et al. 1984), with a temperature of polar dust to 100 K (Mountrichas et al. 2021; Buat et al. 2021) and the emissivity index of polar dust to 1.6 (Casey 2012). The values for the colour excess of polar dust go from no extinction ( $E(B-V) = 0$ ) to  $E(B-V) = 1.0$  because  $E(B-V)$  cannot be well constrained only from the SED shape (Yang et al. 2020). However, adding  $E(B-V)$  as a free parameter can improve the accuracy of the classification type (Mountrichas et al. 2021).

The ratio of the outer to inner radii of the dust torus  $R_{\text{out}}/R_{\text{in}}$  and the optical depth at  $9.7 \mu\text{m}$   $\tau$  are parameters that both AGN models share. The selection of these values changes in studies similar to this one on AGN galaxies depending on the AGN model used. When using the Fritz model it is common to use  $\tau = 6.0$  and  $R_{\text{out}}/R_{\text{in}} = 60$  (e.g. Vika et al. 2017; Małek et al. 2018; Wang et al. 2020), while for SKIRTOR  $\tau = 7.0$  and  $R_{\text{out}}/R_{\text{in}} = 20$  are often used (e.g. Yang et al. 2020; Mountrichas et al. 2021). We adopted the same values as in the literature, even though the  $\tau$  values can be considered large, with the difference that we used  $R_{\text{out}}/R_{\text{in}} = 30$  for the Fritz model to make it more similar to SKIRTOR. We used the default geometrical parameters (power-law densities) in both models to focus on  $i$ ,  $f_{\text{AGN}}$  and  $E(B-V)$ . Finally, we tested two angle configurations: i) with viewing angles between  $0^\circ$  and  $90^\circ$ , and ii) using typical viewing angles of Type-1 and Type-2 AGNs of  $30^\circ$  (unobscured) and  $70^\circ$  (obscured). This comparison helps us to understand how important the viewing angle input parameter is in X-CIGALE.

In summary, we used the parameters and values given in Table 2 to define the grid of X-CIGALE SED models for the sample of Seyfert galaxies. For the remaining parameters not shown in Table 2, we adopted the X-CIGALE default settings. We decided not to include the X-ray or radio modules due to the lack of homogeneous information for the selected sample of Seyfert galaxies (see Sect. 4.5). We assumed the redshifts from SMB in the SED fits.

### 2.2.2 Cleaning X-CIGALE fits

We ran another setup of X-CIGALE without the AGN module (hereafter No-AGN) in addition to the X-CIGALE setups with AGN models described in Table 2. The No-AGN setups helped us to identify bad-fittings and ambiguous cases where an AGN is not dominant in the SED, even though the galaxies are classified as Seyfert.

X-CIGALE minimises the  $\chi^2$  statistic and produces probability

**Table 2.** X-CIGALE grid parameter values adopted for the modelling described in Section 2.2

Parameter	Values	Description
Star formation history (SFH): Delayed		
$\tau_{\text{main}}$	50, 500, 1000, 2500, 5000, 7500	e-folding time of the main stellar population model (Myr).
Age	500, 1000, 2000, 3000, 4000, 5000, 6000	Age of the oldest stars in the galaxy (Myr).
Single-age stellar population (SSP): Bruzual & Charlot (2003)		
IMF	1	Initial Mass Function from Chabrier (2003).
Metallicity	0.02	Assuming solar metallicity.
Dust attenuation: Calzetti et al. (2000)		
$E(B - V)$	0.2, 0.4, 0.6, 0.8	Color excess of the nebular light for the young and old population.
$E(B - V)_{\text{factor}}$	0.44	Reduction factor for the $E(B - V)$ to compute the stellar continuum attenuation.
Power-law slope ( $\delta$ )	-0.5, -0.25, 0.0, 0.25, 0.5	Slope delta of the power law modifying the attenuation curve.
Dust emission: Dale et al. (2014)		
$\alpha$	1.0, 1.5, 2.0, 2.5, 3.0	Alpha from the power-law distribution in Eq. 1.
AGN models:		
$i$	0 – 90 <sup>a</sup>	Viewing angle (face-on: $i = 0^\circ$ , edge-on: $i = 90^\circ$ ).
$f_{\text{AGN}}$	0.1 – 0.9 in steps of 0.05	Fraction of AGN torus contribution to the IR luminosity in Eq. 2
$E(B - V)_{\text{polar}}$	0.0, 0.03, 0.1, 0.2, 0.3, 0.4, 0.6, 1.0	$E(B - V)$ of polar dust (fig 4 of Yang et al. (2020)).
$T_{\text{pd}}$	100	Temperature of polar dust (eq. 10 of Yang et al. (2020)).
$\beta_{\text{pd}}$	1.6	Emissivity index of polar dust (eq. 10 of Yang et al. (2020)).
Fritz model (Fritz et al. (2006))		
$R_{\text{out}}/R_{\text{in}}$	30.0	Ratio of the outer to inner radii of the dust torus.
$\tau$	6.0	Optical depth at 9.7 $\mu\text{m}$ .
$\beta$	-0.50	Beta from the power-law density distribution for the radial component of the dust torus (eq. 3 of Fritz et al. (2006)).
$\gamma$	4.0	Gamma from the power-law density distribution for the polar component of the dust torus (eq. 3 of Fritz et al. (2006)).
Opening Angle ( $\theta$ )	100.0	Full opening angle of the dust torus (fig 1 of Fritz et al. (2006)).
SKIRTOR model (Stalevski et al. (2016))		
$R_{\text{out}}/R_{\text{in}}$	20.0	Ratio of the outer to inner radii of the dust torus.
$\tau$	7.0	Optical depth at 9.7 $\mu\text{m}$ .
$p$	1.0	Power-law exponent of the radial gradient of dust density (eq. 2 of Stalevski et al. (2012)).
$q$	1.0	Angular parameter for the dust density (eq. 2 of Stalevski et al. (2012)).
$\Delta$	40	Angle between the equatorial plane and edge of the torus (half opening angle).

<sup>a</sup> We covered viewing angles between 0° and 90° in steps of 10°. We used the values closest to the predefined angle grid in X-CIGALE. For other setups, we used only 30° and 70°, taking into account that  $i = 90 - \psi$  (with  $\psi$  the angle between equatorial axis and line of sight).

distribution functions for the grid parameters by assuming Gaussian measurement errors (Burgarella et al. 2005; Noll et al. 2009; Serra et al. 2011). In Fig. 2, we show an example of the SED fitting in one of the galaxies (Mrk 662) using the five different setups: smooth torus (Fritz setup from now on), smooth and clumpy torus (SKIRTOR setup from now on), smooth and clumpy torus with only two viewing angles (Fritz 30/70 and SKIRTOR 30/70 setups), and a model without AGN (No-AGN setup). The No-AGN setup (upper-right panel) shows a significant difference with the AGN setups in terms of reduced  $\chi^2$  ( $\chi_{\text{red}}^2$ ), which is expected as an AGN model is needed for most of our Seyfert galaxies. However, in some cases, No-AGN setup have a lower or equal  $\chi_{\text{red}}^2$  than AGN setups, meaning a worse fit with the AGN setup and/or a non-dominant AGN. Another slight difference in these SEDs is the contribution from the AGN (green dashed line) at 10  $\mu\text{m}$ , which varies depending on the best-fitting to a given setup. These differences can play a role in some physical parameters (e.g. attenuation), that may affect the classification type.

We compare the  $\log(\chi_{\text{red}}^2)$  distribution for the SED setups in Fig. 3.

There is a small difference in  $\chi_{\text{red}}^2$  between AGN setups (Fritz and SKIRTOR), with an average value of  $\Delta\chi_{\text{red}}^2 = 0.147$ , which shows that both setups fit the data similarly. Besides, we found that AGN and No-AGN setups have an average difference in  $\log(\chi_{\text{red}}^2)$  of  $\sim 0.4$  dex, favouring AGN setups. For the No-AGN setup, if we use the same  $f_{\text{AGN}}$  value as in the AGN setups (which by construction have a  $f_{\text{AGN}} = 0$ ), then we can compare the difference in  $\chi_{\text{red}}^2$  when adding an AGN model in the SED. We found the smallest  $\chi_{\text{red}}^2$  differences at  $f_{\text{AGN}}$  below 0.2, while the largest differences are at  $f_{\text{AGN}} \sim 0.7$ , when comparing the setups with and without AGN. For the SED setups with AGN, we found that galaxies with  $f_{\text{AGN}}$  between 0.2 and 0.8 have  $\chi_{\text{red}}^2$  values close to one. Therefore, for most galaxies outside this  $f_{\text{AGN}}$  range have poorer fittings. This difference shows the importance of adding the AGN model in the SED fitting and how  $\chi_{\text{red}}^2$  changes for non-dominant AGNs ( $f_{\text{AGN}} < 0.2$ ) and highly-dominant AGNs ( $f_{\text{AGN}} > 0.85$ ).

To better compare the No-AGN and AGN setups, we use the

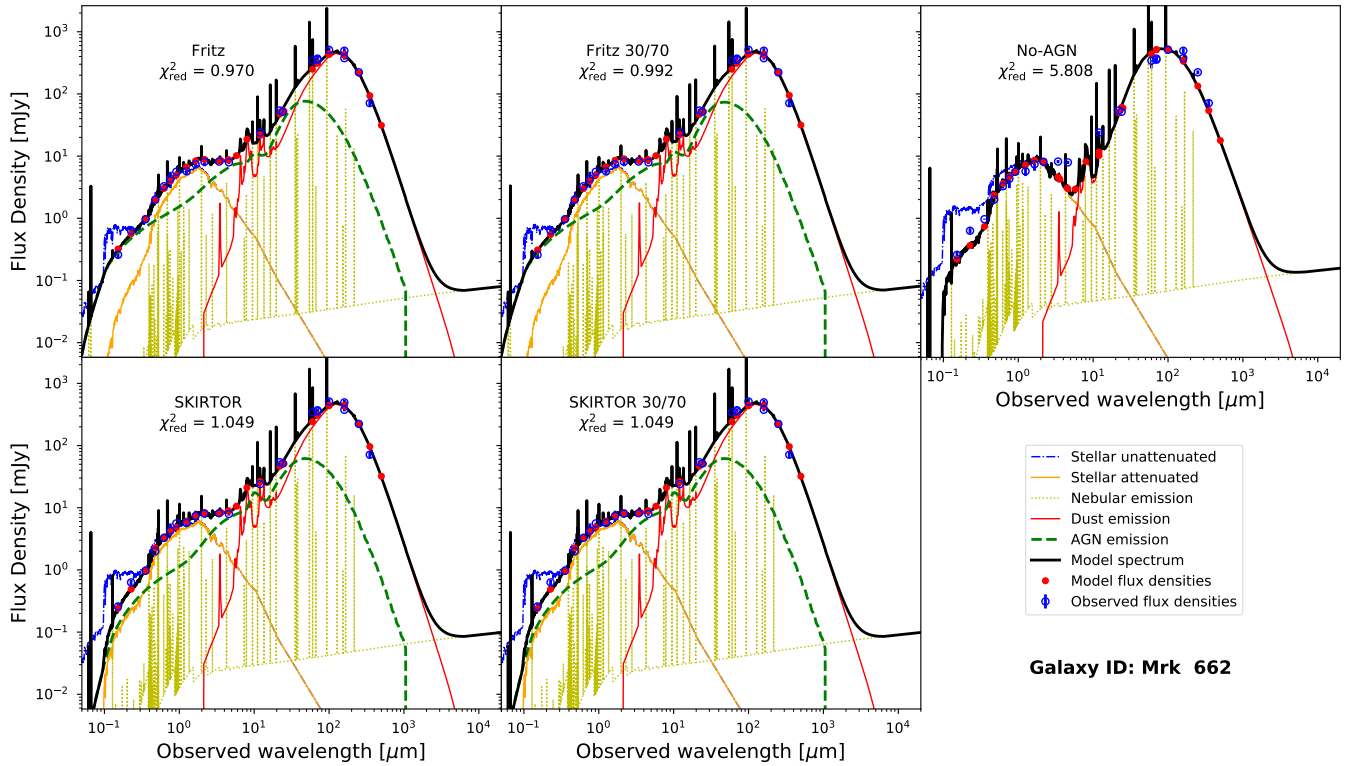


**Figure 2.** Example SEDs of the five SED fitting setups used in this work for the galaxy Mrk 662 at  $z = 0.05$ . No-AGN setup (upper-right panel) usually have higher reduced  $\chi^2$  ( $\chi^2_{\text{red}}$ ) values than AGN setups (other four panels). Each plot contains the contribution to the model spectrum (black line) of: nebular emission (gold dotted lines), attenuated (orange) and non-attenuated stellar emission (blue dot-dashed), dust emission (red solid), and AGN emission (green dashed). The red dots are the best model flux densities and the blue squares mark the observed flux densities with  $1\sigma$  error bars.

Bayesian Inference Criterion (BIC) to see if the AGN module is preferred for the fits, as in other CIGALE works (e.g. [Buat et al. 2019](#)). The BIC is defined as  $\text{BIC} = \chi^2 + k \times \ln(N)$ , with  $k$  the number of free parameters and  $N$  the number of data points used for the fit ([Ciesla et al. 2018](#)) and works as an approximation of the Bayes factor ([Kass & Raftery 1995](#)). Then, the difference between the setups can be calculated as  $\Delta\text{BIC} = \chi^2_{\text{AGN}} - \chi^2_{\text{No-AGN}} + \ln(N)$ , as we are just fixing the  $f_{\text{AGN}}$  to zero in the No-AGN setup. We adopt a positive evidence criterion for No-AGN setup ([Salmon et al. 2016](#)), meaning that galaxies with a  $\Delta\text{BIC} \geq 2$  will prefer the No-AGN setup.

We imposed some constraints in the X-CIGALE estimated values to clean the set of derived parameters for this work. First, we used galaxies with a  $\log(\chi^2_{\text{red}})$  between -0.5 and 0.5 (grey dashed lines in Fig. 3) to avoid over and underestimations, respectively. Second, we selected galaxies where the AGN setups were preferred i.e.  $\Delta\text{BIC} < 2$ . Finally, we selected galaxies where their estimated  $1\sigma$  error in SFR was below one dex, to obtain reliable SFR estimations. Unfortunately, this last selection causes a bias against quiescent galaxies. These constraints led us to remove between 4 757 and 5 181 galaxies (depending on the AGN setup), from which: 69–75% galaxies were over or underestimated fits, 9–15% galaxies had a better fit with the No-AGN setup, and 31–38% galaxies where SFR was not well constrained.

To summarise, we present in Table 3 the total number of galaxies of the original samples (SMB and VCV), samples with photometry that meet our criteria for the SED fitting procedure, and the well-constrained fits with the X-CIGALE AGN models with respect to

their Seyfert classification. In Appendix B, we verify the quality of the fits for the main parameters studied in this work and the parameter space used for the fitting procedure by mock analysis. The mock analysis is a standard procedure included inside the CIGALE. A detailed description of this process can be found in [Boquien et al. \(2019\)](#).

### 2.2.3 Verification with other estimates

We verified the estimates from our procedure by comparing with a similar study done with CIGALE by [Vika et al. \(2017\)](#). [Vika et al. \(2017\)](#) uses a sample of 1 146 galaxies selected from the CASSIS spectroscopic sample ([Lebouteiller et al. 2015](#)) with good photometric coverage from UV to mid-IR in the redshift range  $0 < z < 2.5$ . As all these galaxies have been observed with *Spitzer*/IRS, the sample is biased to significantly brighter mid-IR galaxies. There are two main differences between the estimated physical parameters from [Vika et al. \(2017\)](#) and this work. The first difference is the way the photometry was retrieved. [Vika et al. \(2017\)](#) used specific catalogues that contain broad-band photometry for their sample of galaxies, while in this work we use data available in CDS and NED. Thus, we include additional information as the databases collect more broad-band photometry. The second difference is the assumed grid values for the SED modelling. Although the numerical values in most of the input parameters are not the same, here we mention the three most important differences between the grids. First, the IMF in this work comes from [Chabrier \(2003\)](#), while [Vika et al. \(2017\)](#) uses the IMF from [Salpeter \(1955\)](#). The use of the Chabrier IMF will lead to lower

**Table 3.** Summary of the Seyfert samples used in this work. The original samples of Seyfert galaxies are in columns 2 (VCV) and 3 (SMB). Galaxies with photometry from the samples fulfilling our criteria are in column 4. The last four columns show the final counts for well-constrained SEDs in X-CIGALE. We show the counts from VCV and SMB classifications in columns 4-8 for Sy1, Sy2 and unclassified Seyfert rows. We show the counts for VCV classification for intermediate or other Seyfert galaxies. The last row shows the total number of galaxies in each of the samples.

Seyfert Classification	Samples		With Photometry	X-CIGALE AGN models			
	VCV	SMB		SKIRTOR	Fritz	SKIRTOR 30/70	Fritz 30/70
Seyfert 1	13 177	13 760	8 942 / 9 421	5 913 / 6 328	6 295 / 6 683	6 064 / 6 453	6 350 / 6 723
Seyfert 2	4 567	5 040	3 284 / 3 679	1 473 / 1 626	1 535 / 1 697	1 390 / 1 544	1 361 / 1 515
Unclassified Seyfert	87	121	54/73	27 / 38	28 / 36	25 / 34	28 / 37
Intermediate Seyfert	920	...	756	507	489	492	479
Alternative Seyfert	170	...	137	72	69	60	57
Total galaxies	18 921	18 921	13 173	7 992	8 416	8 031	8 275

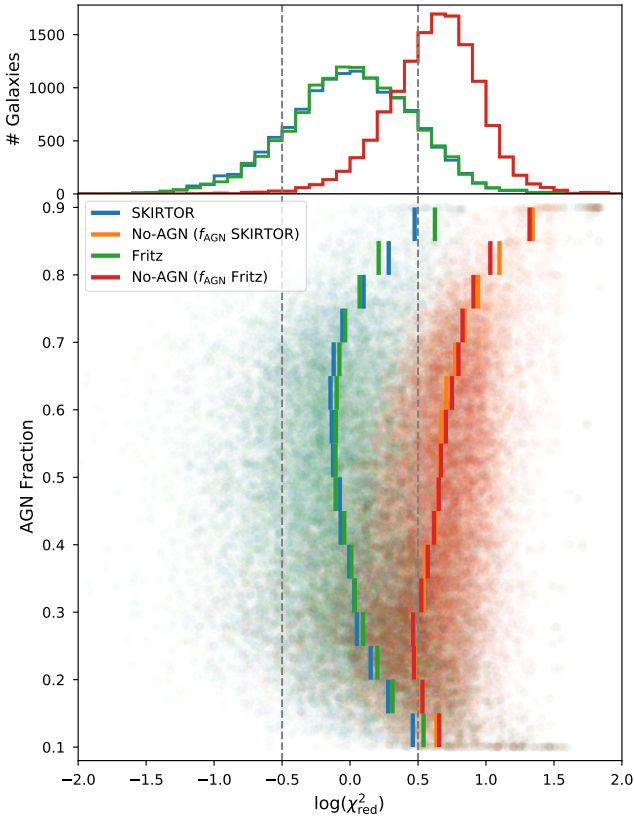


**Figure 3.** Reduced-chi-square ( $\chi_{\text{red}}^2$ ) distribution for the setups used in this work. *Upper-panel:* histogram of the  $\chi_{\text{red}}^2$  distribution for SKIRTOR (blue), Fritz (green) and No-AGN (red) setups. *Bottom-panel:*  $\chi_{\text{red}}^2$  against the estimated AGN fraction ( $f_{\text{AGN}}$ ) for each galaxy (shaded dots) and the running median in bins of  $f_{\text{AGN}}$  values (solid lines). No-AGN setup ( $f_{\text{AGN}} = 0$ ) is plotted assuming the  $f_{\text{AGN}}$  values of the AGN setups, thus showing slightly different median values with Fritz and SKIRTOR setups. We assumed that well fitted galaxies have a  $\log(\chi_{\text{red}}^2)$  between -0.5 and 0.5 (grey dashed lines).

stellar mass values in this work with respect to Vika et al. (2017). Second, the parameter space for  $f_{\text{AGN}}$  in this work is finer sampled and more homogeneously distributed than the one from Vika et al. (2017). And third, the selected viewing angles for the AGN in Vika et al. (2017) are only  $i = 0^\circ$  and  $i = 90^\circ$  for the Fritz AGN model.

We selected the smooth torus model with two viewing angles (Fritz 30/70 setup) to compare the results from Vika et al. (2017), as it is

the most similar model in this work. We cross-matched the Vika et al. (2017) catalogue with the Fritz 30/70 setup between  $3''$  and we found 87 galaxies for the comparison in the range of  $0.02 < z < 1.4$ , with a median of  $z = 0.13$ . In Fig. 4, we present the comparison of six physical parameters between this work and Vika et al. (2017). In terms of SFR, AGN luminosity and dust luminosity, there is no clear difference between the estimates, the small systematic offsets are related to the different assumed values of the grid. For example, in both works the dust model from Dale et al. (2014) is used to estimate the dust luminosity, which depends mainly on the power-law parameter  $\alpha$  of the mass distribution (Eq. 1). In Vika et al. (2017), they only use two values for  $\alpha$ , while in this work we use five. On the contrary, the estimates on stellar mass are lower in this work mainly due to the adopted IMF, but the estimated median errors are similar between both works.

Age and  $f_{\text{AGN}}$  are the only physical parameters that are very different from Vika et al. (2017). In the case of  $f_{\text{AGN}}$ , the estimates are constrained by the different grid selection. However, the estimated median error is lower in this work than in Vika et al. (2017), as we use more photometric bands and a finer  $f_{\text{AGN}}$  grid. In the case of the age, Vika et al. (2017) noted that age estimates are not well constrained in CIGALE, besides the differences in the grid values. This problem is also obvious from our estimates, which have uncertainties similar to those presented by Vika et al. (2017). In general, the physical parameters estimated in Vika et al. (2017) are similar to those presented in this work, validating our approach of obtaining data directly from astronomical databases.

## 3 RESULTS

### 3.1 Feature selection

Recent advances in algorithms and machine learning techniques are helping to classify very complicated physical systems (Carleo et al. 2019; Virtanen et al. 2020). These classification tasks have covered the full range of galactic and extragalactic sources (e.g. Tamayo et al. 2016; Miettinen 2018; Jayasinghe et al. 2018; Bluck et al. 2020; Baqui et al. 2021). Nowadays, these methods are helping to classify astrophysical objects not only from reduced fluxes, but also from astronomical imaging surveys, where Type-1 AGN are separated from normal galaxies (Golob et al. 2021). Therefore, joining X-CIGALE physical parameters with these classification techniques could be useful to solve the AGN ‘‘zoo’’ of galaxies for different AGN scenarios.

However, X-CIGALE estimates more than 60 physical parameters depending on the number of modules included in the SED fitting.

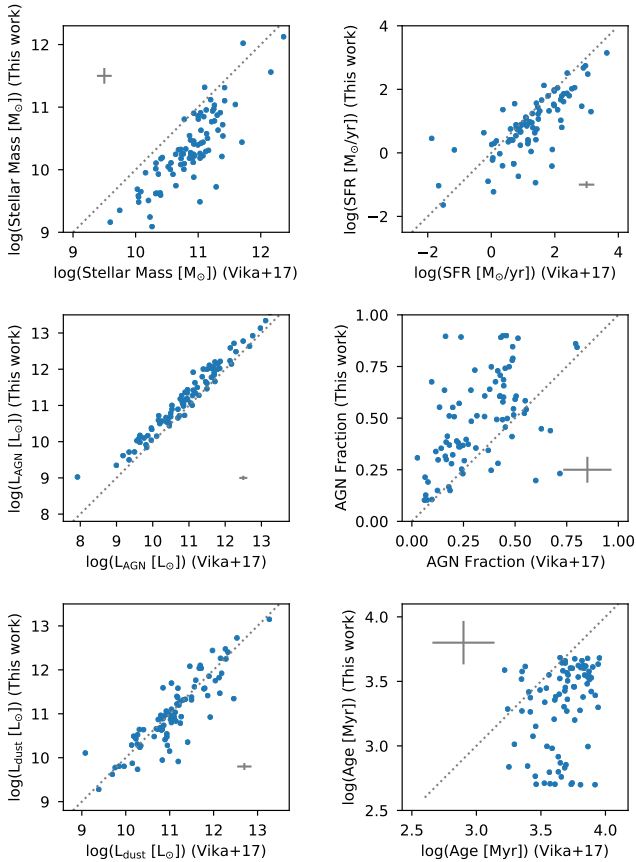


**Figure 4.** Comparison between the estimated physical parameters from this work and by Vika et al. (2017). The pointed line represents the 1:1 relation. The grey crosses represent the median estimated error for each of the parameters. In general, the estimates from this work agree with the results presented by Vika et al. (2017). Based on the median estimated errors, our results are better constrained than the ones from Vika et al. (2017).

Therefore, it is necessary to select a smaller number of physical parameters which are the most informative for a classification task. We use a set of 29 737 estimates from the sum of the four X-CIGALE AGN setups (SKIRTOR, Fritz, and their respective 30/70 setups), where VCV and SMB share the same classification of Sy1 or Sy2. We split this set randomly into train and test subsets with a proportion of 80% and 20%, respectively. Then, we scale the subsets by subtracting the median and transforming according to the interquartile range. We perform this scaling to obtain classifications that are robust against outliers. We discard physical parameters directly related to inputs (e.g. redshift) and those dividing old and young stellar populations (e.g. old and young stellar masses).

We implement two machine learning ensemble techniques for the classification task: random forest and gradient boosting. Both ensemble techniques provide estimates using multiple estimators. The first technique is composed of a collection of trees randomly distributed where each one decides the most popular class (Breiman 2001). While the second technique takes into account “additive” expansions in the gradient descent estimation to improve the selection of the class (Friedman 2001). For the random forest we use the `scikit-learn` (Pedregosa et al. 2012) classifier `RandomForestClassifier`. For the gradient boosting we use the `XGBoost` (Chen & Guestrin 2016) classifier `XGBClassifier`. We tune the classifier’s parameters us-

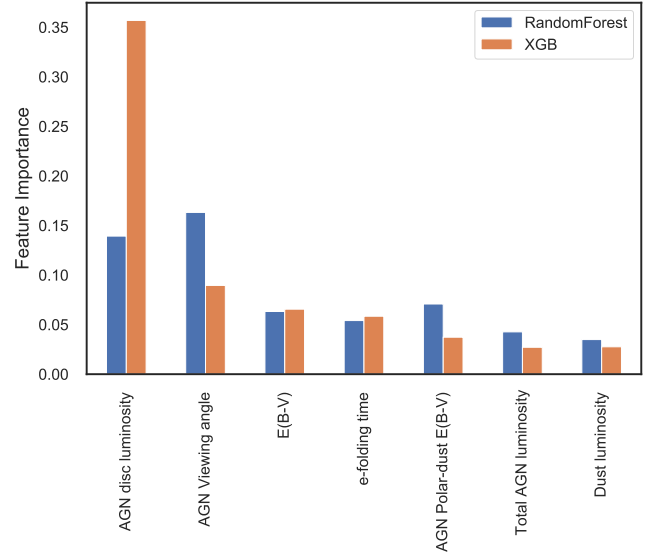


**Figure 5.** Feature importance scores for the seven most important physical parameters in both `RandomForestClassifier` and `XGBClassifier`. Parameters with scores below 0.03 (i.e. < 3%) are not presented. The observed AGN disc luminosity is the most important physical parameter to describe Seyfert types.

ing an estimator from `scikit-learn` that uses cross-validation in a grid-search `GridSearchCV`. The grid is defined with two parameters: the number of trees in the forest `n_estimators`, and the maximum depth of the tree `max_depth`. Values in the grid for `n_estimators` cover the range between 100 and 500 in steps of 100, while for `max_depth` the values cover the range between 10 and 40 in steps of 5. We use the F1-score to evaluate the predictions on the test set. The F1-score is the harmonic mean of precision and recall, where precision is the fraction of true positives over true and false positives and recall is the fraction of true positives over true positives and false negatives. With the `GridSearchCV` estimator, the best values for the `RandomForestClassifier` are `n_estimators` = 200 and `max_depth` = 25, while for `XGBClassifier` are `n_estimators` = 300 and `max_depth` = 25.

We apply a recursive feature elimination and cross-validation selection (RFECV) to select the ideal number of physical parameters to study. We perform 10 k-fold cross-validations with `RandomForestClassifier` and `XGBClassifier`. In Figure 5, we present the feature importance (the score of a feature in a predictive model) for both classifiers after the RFECV has been applied. We find that five physical parameters contribute the most in the classification task. These physical parameters are observed AGN disc luminosity, AGN viewing angle, AGN polar dust  $E(B - V)$ , e-folding time ( $\tau_{\text{main}}$ ), and the colour excess. Though we find that the feature importance is low for SFR and  $f_{\text{AGN}}$ , the classification scores improve when we include these parameters, which are important when comparing to observational results. Thus, we decided to focus on these previous seven parameters to assess the impact of the viewing angles in the samples of Seyfert galaxies. In Sect. 4.1, we describe the role that these physical parameters play in the classification task.

It is necessary to clarify here that the  $L_{\text{AGN}}^{\text{disc}}$  is the observed total luminosity of the accretion disc in X-CIGALE. The AGN accretion power is the term we use to refer to the intrinsic luminosity of the accretion disc.

### 3.2 Comparison of X-CIGALE outputs from different SED fitting setups

We compare the seven selected physical parameters using the density distribution of the selected setups and Seyfert type samples. We quantify the difference between the distributions using the two-sample Kolmogorov–Smirnov (KS) test. The KS test checks the null hypothesis that two distributions are drawn from the same underlying distribution. We reject the null hypothesis if  $D$  (the distance between cumulative distributions) is higher than the critical value at a significance level of  $\alpha = 0.05$  (e.g.,  $P < 0.05$ ). We visualise the distributions using a bandwidth of the density estimator following the Scott’s Rule (Scott 2015). The visualisation and the KS statistics  $D$  tell us how different the samples are.

#### 3.2.1 AGN setup comparison

We compare the AGN setups (SKIRTOR, Fritz, and their respective 30/70 setups) before comparing the results between different Seyfert types. We present the probability distribution functions for the parameters and their errors in Fig. 6.

First, we check the differences between the setups covering all viewing angles and setups with viewing angles of only  $30^\circ$  and  $70^\circ$ . We do not observe a clear difference between these two sets of setups in most of the physical parameters. Their main discrepancy in the distributions is in the viewing angle, as expected. In setups with  $30^\circ$  and  $70^\circ$ , we find galaxies with viewing angles around  $50^\circ$ . These values are related to the Bayesian nature of the estimations, as seen in the estimated error. Something different happens in setups with the full range of viewing angles used for the SED modelling. The distribution of the viewing angle peaks at around  $20^\circ$  while at larger angles ( $\geq 45^\circ$ ) the distribution is almost flat.

Second, we check the differences between SKIRTOR and Fritz setups. In this case, small differences are noticeable in some physical parameters (e.g. observed AGN disc luminosity and polar dust). However, both kinds of setups follow similar trends in all parameters. If we observe estimated errors, all of them are well constrained, partly due to our  $\chi^2_{\text{red}}$  selection criteria.

Finally, the null hypothesis in the KS test is almost always rejected in all the setups. The only cases where the null hypothesis cannot be rejected are at Fritz and Fritz 30/70 setups for the  $\tau_{\text{main}}$  and SFR parameters ( $D \sim 0.02$ ,  $P \sim 0.7$ ), and at SKIRTOR and SKIRTOR 30/70 setups for the SFR parameter ( $D \sim 0.02$ ,  $P \sim 0.1$ ). We find  $D < 0.1$  in most parameters when comparing all setups except for the viewing angle due to the way we designed the setups, as expected. Variations in the setups will only give different individual results, but in general, the setups will be similar when interpreting the physical results in Seyfert galaxies.

#### 3.2.2 Seyfert types 1 and 2 comparison

According to the AGN unified model, the viewing angle is the main physical parameter to classify Seyfert galaxies into Type-1 AGNs (face-on) and Type-2 AGNs (edge-on). In X-CIGALE, SED models which include AGN follow the AGN-unification scheme (Yang et al. 2020). The viewing angle estimated by the models should coincide with the classification scheme of Sy1 and Sy2 galaxies. For this analysis, we use galaxies where Seyfert classifications from VCV and SMB agree. In Fig. 7, we present the probability distribution functions for the seven selected parameters now separating the galaxies in Sy1 and Sy2 for the SKIRTOR and Fritz setups. The distribution of viewing angles for Sy1 coincides with the expected low values

of face-on galaxies. For Sy2 galaxies, the viewing angle distribution extends over a wide range of angles, but agrees with a viewing angle close to edge-on galaxies.

KS statistic values  $D$  show: i) independent of the used AGN setup, the distributions of the parameter values are similar for the same Seyfert galaxy types, and ii) the different Seyfert types can be well separated as the distributions are different for both setups. The only exception is in terms of the  $E(B-V)$ , where  $D$  values for Sy1 galaxies depend on the used setup.

In terms of  $f_{\text{AGN}}$ , Sy2 galaxies have mainly lower values than Sy1 galaxies. We observe something similar for the parameters of SFR and e-folding time ( $\tau_{\text{main}}$ ), with low values typically associated to Sy2 galaxies. Although for these two parameters, the difference with Sy1 could be due to the strong UV / optical emission that bias these parameters. Values of the polar-dust show that in Sy2 galaxies the emission is obscured, in contrast to the Sy1 where  $E(B-V) = 0$  is more common.

The most interesting result in this comparison is the significant difference in the  $L_{\text{AGN}}^{\text{disc}}$  between the two Seyfert types. Most Sy2 have  $L_{\text{AGN}}^{\text{disc}}$  below  $\sim 10^{10} L_{\odot}$ . The opposite happens for Sy1 galaxies where most  $L_{\text{AGN}}^{\text{disc}}$  are above  $\sim 10^{10} L_{\odot}$ . This result is also verified with the KS statistic  $D$ , where higher  $D$  values are found when comparing Sy1 and Sy2 samples for  $i$  and  $L_{\text{AGN}}^{\text{disc}}$ . In a classification task, this latter physical parameter might be more informative than others, as we have seen with the feature importance score (Sect 3.1 and Fig. 5). We test this idea when predicting the classification type in unclassified and discrepant Seyfert galaxies (Sect. 3.5).

We verify the impact of missing bands in the SED fitting in our sample of galaxies for the estimated parameters. The differences we found between the probability density functions with and without a given band can be explained by the way the Seyfert types are distributed in the sample. For example, in the 2MASS bands, a third of the galaxies detected in these bands are classified to be Seyfert 2, while in the cases where we do not have these bands most of the galaxies ( $\sim 90\%$ ) are of Seyfert 1 type. Most of the galaxies not detected by 2MASS follow the trends of Seyfert 1 galaxies, with high AGN disc luminosities, lower viewing angles and polar dust close to zero. This shows that even if some bands are missing, the SED fitting procedure still gives similar values for the physical parameters compared to other galaxies which have the same classification. In other words, the lack of some data does not necessarily impact the results of this work significantly, but it could be important in individual cases, which is out of the scope of this work.

#### 3.2.3 Intermediate Seyfert types comparison

From the results presented in Figs. 6 and 7, we observe a small difference between the AGN setups. Thus, we select the SKIRTOR setup to visualise the difference between intermediate Seyfert types. These intermediate galaxy types are classified in subgroups following Osterbrock (1977, 1981) with the quantitative approach of Winkler (1992). The subgroups are divided using the ratio between  $H\beta$  and  $[O\text{III}]$  fluxes ( $R$ ) and the spectral profiles of the Balmer lines (see also Véron-Cetty & Véron (2010)). In this classification scheme Seyfert galaxies are: Sy1.0 if  $R > 5$ , Sy1.2 if  $2.0 < R < 5.0$ , Sy1.5 if  $0.33 < R < 2.0$ , Sy1.8 if  $R < 0.33$  with a broad component in  $H\alpha$  and  $H\beta$ , and Sy1.9 if the broad component is visible in  $H\alpha$  but not in  $H\beta$ .

We show in Fig. 8 the probability density functions of the physical parameters for the intermediate Seyfert types. Interestingly, these intermediate types coincide with the picture observed in Sy1

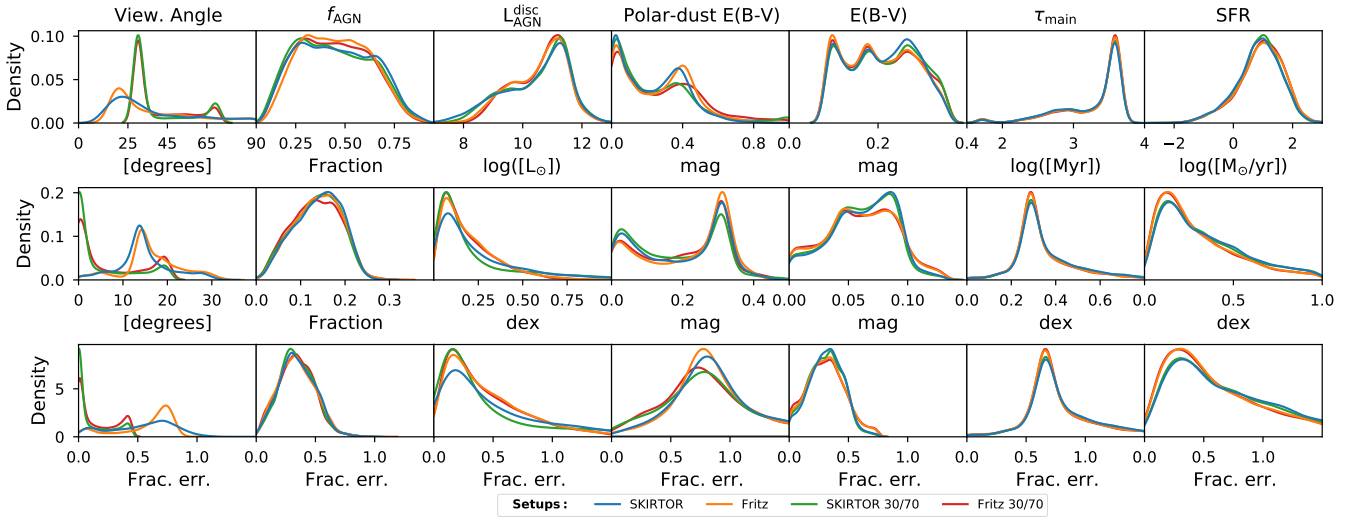


**Figure 6.** Probability density functions for the estimated parameters (upper panels), their respective errors (middle panels) and their relative fractional errors (lower panels). We compare the SKIRTOR (blue), SKIRTOR 30/70 (green), Fritz (orange), and Fritz 30/70 (red) setups. The difference between the setups that use the full range of viewing angles (SKIRTOR and Fritz) and those that use only two angles (30/70 setups) is significant only in the viewing angle, as expected.

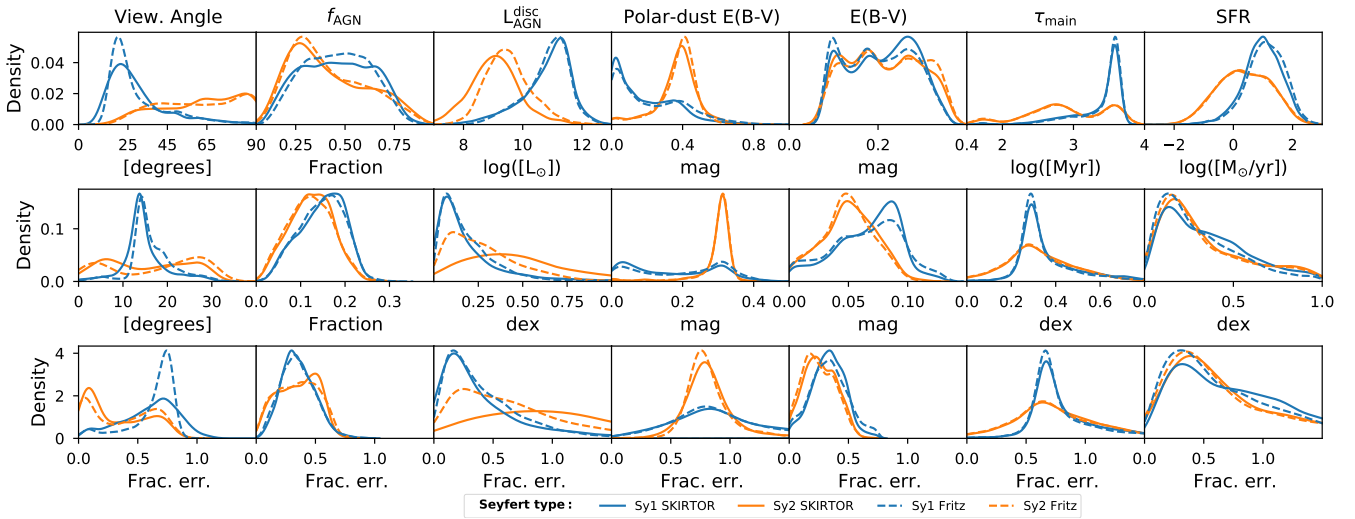


**Figure 7.** Probability density functions for the estimated parameters (upper panels), their respective errors (middle panels) and their relative fractional errors (lower panels). We compare the Seyfert types 1 (blue) and 2 (orange) for the SKIRTOR (solid) and Fritz (dashed) setups. A clear difference is observed in some of these parameters between Sy1 and Sy2 (e.g. viewing angle, polar dust  $E(B - V)$  and observed AGN disc luminosity).

and Sy2 in most of the physical parameters. In some parameters, a possible numerical sequence from Sy1 to Sy2 can be observed (Sy1.0>Sy1.2>Sy1.5>Sy1.8>Sy1.9). Three parameters show this sequence in their KS statistic  $D$  values: viewing angle, observed AGN disc luminosity and the polar dust  $E(B - V)$ . For the viewing angle  $i$ , Sy1.0, Sy1.2 and Sy1.5 tend to estimate values around  $25^\circ$ , while for Sy1.8 and Sy1.9 there are more  $i$  values above  $45^\circ$ . For the  $L_{\text{AGN}}^{\text{disc}}$ , the density functions for Sy1.8 and Sy1.9 peak below  $10^{10} L_\odot$ , Sy1.5 peaks at  $\sim 10^{10} L_\odot$ , and Sy1.2 and Sy1.0 peak at values above  $\sim 10^{10} L_\odot$ . The polar dust in Sy1.0 and Sy1.2 shows in general no extinction, Sy1.5 shows mild values (0.1-0.3), and Sy1.8 and Sy1.9 peak at around 0.4. These results agree with the expected behaviours of the transition between Sy1 and Sy2 type galaxies.

Other physical parameters (e.g.  $f_{\text{AGN}}$  or  $\tau_{\text{main}}$ ) also show similarities between close intermediate Seyfert types, but not as clear as the parameters described before. This suggests that AGN SED models, as the ones available in X-CIGALE, can estimate the possible transitional phase between different Seyfert types. In Sect. 4.2, we discuss a possible explanation for this transitional phase. In addition, in Sect. 4.4, we discuss the effect of using these AGN classifications when interpreting our results.

### 3.3 Redshift behaviour/evolution

Separating Seyfert galaxies in Type-1 or Type-2 is very important to understand the nature of these types of galaxies. In previous section (Sect. 3.2), we notice that some physical parameters could be used

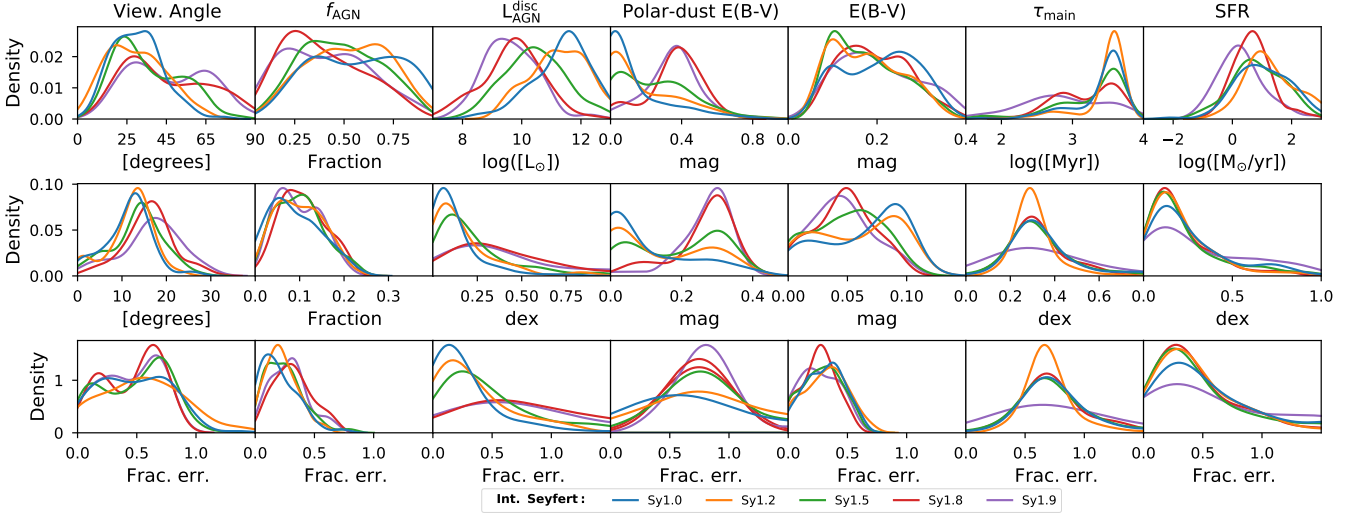


**Figure 8.** Probability density functions for the estimated parameters (upper panels), their respective errors (middle panels) and their relative fractional errors (lower panels). We compare the intermediate Seyfert types 1.0 (blue), 1.2 (orange), 1.5 (green), 1.8 (red), and 1.9 (purple) for the SKIRTOR setup. A transition between Sy1 and Sy2 galaxies is observed in the viewing angle, polar dust  $E(B - V)$  and observed AGN disc luminosity.

to separate the two Seyfert types. Now, we verify if the separation between Seyfert types holds and/or evolves with redshift. In Fig. 9, we present the evolution of the SED physical parameters as a function of redshift. For this figure, we use estimates from the SKIRTOR setup and separate the Seyfert types using the classifications from SMB.

In the upper panel of Fig. 9, we notice that the number of classified Sy2 galaxies are almost always below the number of classified Sy1 galaxies. Most of these classifications come from redshifts below  $z \sim 0.5$ , where spectroscopic information of the local Universe is more readily available, compared to high redshift galaxies. In the lower panels, the median of the physical parameters is similar between the two Seyfert types for  $f_{\text{AGN}}$ ,  $E(B - V)$ ,  $\tau_{\text{main}}$  and SFR. However, the estimated values for the viewing angle, observed AGN disc luminosity and polar dust separate the two Seyfert types.

The viewing angle does not evolve with redshift, as expected. In general, the viewing angle for Sy1 galaxies is mostly located at  $\sim 25^\circ$  while for Sy2 galaxies is at  $\sim 65^\circ$ . Thus, we can use the value of  $45^\circ$  to separate the two types of Seyfert galaxies. For  $L_{\text{AGN}}^{\text{disc}}$ , the difference is always above 0.8 dex (at  $z \sim 0$ ) and can go up to  $\sim 2.3$  dex at  $z \sim 0.43$ . We define a separation limit with the median values of the separation between Seyfert type as linear relation

$$\log \left( L_{\text{AGN}}^{\text{disc}} \right) = (9.20 \pm 0.08) + (8.67 \pm 0.61) \times \log(1 + z), \quad (3)$$

where  $z$  is redshift. Finally, for the polar dust, the minimum difference of  $\sim 0.1$  occurs at  $z < 0.1$  and increases with redshift because most of the Sy2 galaxies above  $z = 0.2$  have an estimate of 0.4 compared to values close to zero in Sy1, as expected. We do not define a separation for the polar dust due to the similarity of the estimates at  $z < 0.1$ .

These three parameters (viewing angle, observed AGN disc luminosity and polar dust) are tightly related in X-CIGALE (Yang et al. 2020). However, polar dust have larger uncertainties in the estimations, as show in Figs. 6–8. On the other side,  $L_{\text{AGN}}^{\text{disc}}$  could be a more robust parameter in classification tasks than the viewing angle. In Sy1 galaxies the median contribution from the observed disc luminosity to the total AGN luminosity is  $\sim 52\%$ , while for Sy2 the median contribution is around  $\sim 4\%$ . Furthermore, as we see in Figs. 7 and 8, the separation is more evident between Seyfert types in observed AGN

disc luminosity than in the viewing angle. The extent of the viewing angles and their uncertainties for Sy2 galaxies calls into question the use of this parameter to assess type in SED models.

### 3.4 Classifiers in Seyfert galaxies

We compare different classifiers to test if the physical parameters estimated by the SED modelling are useful to classify AGN galaxies. We define two different scenarios to do the classifications: i) using individual X-CIGALE physical parameters, ii) using ensemble methods with X-CIGALE selected physical parameters. For the first scenario, we use the two limits defined for  $i$  and  $L_{\text{AGN}}^{\text{disc}}$ ,  $i = 45^\circ$  and Eq. 3 respectively, as illustrated in Fig. 9. For the second scenario, we use two machine learning ensemble methods: RandomForestClassifier and XGBoostClassifier, to be consistent with the assumptions in the initial selection of physical parameters (Sect. 3.1). In the second scenario, we randomly split the sample of galaxies in train and test sets with a contribution of 80% and 20%, respectively. We use three different metrics to compare and test the quality of these binary classifications: Matthews correlation coefficient (MCC, Matthews 1975), F1-score and accuracy. MCC is the correlation coefficient between observed and predicted classifications, the F1-score is the harmonic mean of precision and recall (as described in Sect. 3.1), while accuracy is the fraction of samples correctly classified. These metrics are usually used in binary classifications, however they can be sensitive to imbalanced data (Tharwat 2020). Thus, we assess the scenarios by defining a baseline using the DummyClassifier from scikit-learn. This classifier respects the class distribution (i.e. stratified with Seyfert types) and generates random predictions, so it works as a sanity check. Therefore, we use five classifiers with three metrics to test the classification methods.

We use the subset of Seyfert galaxies where the classifications (of Type-1 and Type-2) were the same. We apply the different classifiers described previously for each AGN setup and present their metrics in Table 4. We notice that all classifiers outperform the baseline. In general, the best AGN setup in all the classifiers is SKIRTOR 30/70. In the scenario where we use individual X-CIGALE physical param-

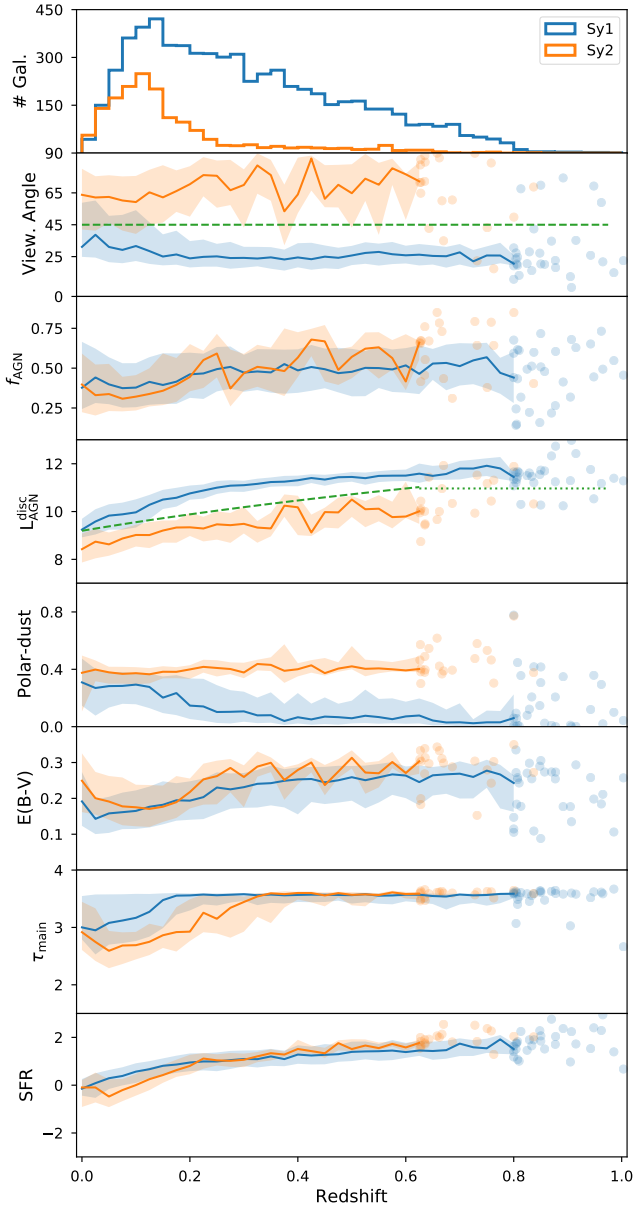


**Figure 9.** Redshift evolution of the physical parameters for the sample of Seyfert galaxies using the SKIRTOR setup. In the uppermost panel, we present the histogram of the Sy1 and Sy2 galaxies in terms of redshift. At redshift higher than 0.6, we find only a few Sy2 galaxies. At redshift above 0.8, the number of Sy1 galaxies reduces to tens of galaxies. In the rest of the panels, we show the running median of the physical parameters in Sy1 (blue) and 2 (orange), with the range between the 25th and 75th percentiles as shaded regions. We calculate the running median for bins with at least ten galaxies. For bins with fewer than ten galaxies, we plot the galaxies as scatter points. For the viewing angle we include the value of  $i = 45^\circ$  that separates the two Seyfert samples (green dashed line). We also include the separation limit for the two samples using  $L_{\text{AGN}}^{\text{disc}}$ , assuming the linear relation described in Eq. 3 (green dashed line) and a constant of  $\log(L_{\text{AGN}}^{\text{disc}}) = 10.97$  at  $z > 0.6$  (green pointed line). Galaxies with  $z > 1$  are not shown.

**Table 4.** Prediction metrics for galaxies with the same classification in **SMB** and **VCV**. The baseline is defined from a random classifier as mention in the text. In bold, we highlight the highest metric value for a given classifier. In general, the SKIRTOR 30/70 setup is the one that best separates Sy1 and Sy2 galaxies, although SKIRTOR metrics are good too.

Classifier	Setup	Metrics		
		MCC	F1	Accu.
Viewing angle ( $i$ )	SKIRTOR	0.541	0.763	0.827
	Fritz	0.492	0.737	0.808
	SKIRTOR 30/70	<b>0.580</b>	<b>0.781</b>	<b>0.846</b>
	Fritz 30/70	0.530	0.746	0.817
AGN disk luminosity ( $L_{\text{AGN}}^{\text{disc}}$ )	SKIRTOR	<b>0.635</b>	<b>0.808</b>	<b>0.860</b>
	Fritz	0.542	0.769	0.842
	SKIRTOR 30/70	0.621	0.801	<b>0.860</b>
	Fritz 30/70	0.535	0.764	0.848
Random Forest	SKIRTOR	0.717	0.856	0.907
	Fritz	0.732	0.865	0.913
	SKIRTOR 30/70	<b>0.737</b>	<b>0.866</b>	<b>0.914</b>
	Fritz 30/70	0.646	0.822	0.900
XGBoost	SKIRTOR	0.666	0.833	0.896
	Fritz	0.680	0.840	0.898
	SKIRTOR 30/70	<b>0.716</b>	<b>0.857</b>	0.910
	Fritz 30/70	0.707	0.853	<b>0.912</b>
Baseline	All	-0.003	0.499	0.691

eters,  $L_{\text{AGN}}^{\text{disc}}$  is in most cases a better discriminator than the viewing angle  $i$ . In the scenario where we use ensemble methods, both classifiers are similar but better than the  $L_{\text{AGN}}^{\text{disc}}$  and  $i$ , as expected. Part of the success of the SKIRTOR 30/70 AGN setup with individual classifiers is the assumption of using two viewing angles that follows the edge-on and face-on geometrical configurations. However, if  $i$  is the most robust parameter in the classification task, we would also expect higher numbers in the metrics for Fritz 30/70, which is not the case. For the classifier using  $L_{\text{AGN}}^{\text{disc}}$ , we find that most of the metrics between SKIRTOR and SKIRTOR 30/70 are not far from each other. These results mean that  $L_{\text{AGN}}^{\text{disc}}$  in SKIRTOR setups can be used to assess Seyfert type of a galaxy. Nevertheless, this classifier will not achieve as accurate predictions as the ensemble methods used in this work. In Sect. 4.4, we discuss the main drawback of using these classifiers in AGNs with SED models.

### 3.5 Predictions on unclassified and discrepant Seyfert galaxies

We test if the estimation from the  $L_{\text{AGN}}^{\text{disc}}$  and the machine learning classifiers are robust and useful to predict the unclassified and discrepant cases in Seyfert galaxies. We compare the Seyfert type predictions of these classifiers with the literature. We gather information about other activity type classifications, outside **VCV** and **SMB** where possible, and we present this information in Table C1. We discuss the classifications for the 59 galaxies (14 unclassified and 45 discrepant) in the following paragraphs.

First, we focus on unclassified Seyfert galaxies by neither **VCV** nor **SMB**, as shown in Table 5. From the 14 unclassified Seyfert galaxies with the  $L_{\text{AGN}}^{\text{disc}}$  and ML methods: i) one galaxy (6dFGS gJ234635.0-205845) is classified for both methods as Sy2 galaxies, ii) seven are classified for both methods as Sy1 galaxies, and iii) six have mixed classifications in the two methods. From the literature classifications, two galaxies (LEDA 1485346 and MCG+00-11-002) coincides with the Seyfert classification. For MCG+03-45-003, we are not able to

**Table 5.** Classification types in unclassified Seyfert galaxies. The second and third columns show the Seyfert type obtained using the  $L_{\text{AGN}}^{\text{disc}}$  and machine learning ensemble methods, respectively. The fourth column shows the assumed classification from the literature. Finally, the last column shows if the previous classifiers are similar with the AGN type in the literature. In case  $L_{\text{AGN}}^{\text{disc}}$  and ML classifications are different split the last column in two options.

Object ID	Classification type			
	$L_{\text{AGN}}^{\text{disc}}$	ML	Literature	Sim.
2MASX J12140343-1921428	Sy1	Sy1	Mix. blazar	Y
2MASX J18121404+2153047	Sy2	Sy1	–	–
2MASX J21560047-2144325	Sy2	Sy1	–	–
2MASX J23032790+1443491	Sy1	Sy1	Composite	N
6dFGS gJ234635.0-205845	Sy2	Sy2	–	–
CADIS 16-505716	Sy1	Sy1	QSO	Y
ESO 373-13	Sy2	Sy1	–	–
LEDA 1485346	Sy1	Sy1	Sy1	Y
LEDA 3095610	Sy1	Sy1	QSO	Y
LEDA 3096762	Sy1	Sy1	QSO	Y
MCG+00-11-002	– <sup>a</sup>	Sy1	Sy1	–/Y
MCG+03-45-003	– <sup>a</sup>	– <sup>a</sup>	Sy2	–
QSO B1238+6232	Sy2	Sy1	QSO	N/Y
[HB93] 0248+011A	Sy1	Sy1	QSO	Y

<sup>a</sup> The classification changes depending on the AGN setup used.

compare it with our classifiers because classifications change depending on the AGN setup used. In addition, we found a mixed blazar (2MASX J12140343-1921428), five quasar (CADIS 16-505716, LEDA 3095610, LEDA 3096762, QSO B1238+6232 and [HB93] 0248+011A), and a composite galaxy (2MASX J23032790+14434). We assume these seven galaxies cannot be Seyfert galaxies. However, we can compare the prediction’s similarity with Type-1 AGN. For the mixed blazar and quasars (QSO), the  $L_{\text{AGN}}^{\text{disc}}$  and ML methods classify them as Sy1 types (except for QSO B1238+6232 with  $L_{\text{AGN}}^{\text{disc}}$ ), which are close to Type-1 AGNs in the unified model scheme. Thus, 8/14 of the galaxies in the unclassified subset have similar classifications to the AGN type. Therefore, it may be possible to distinguish the AGN type from the classifiers presented in this work.

Second, we focus in the 45 discrepant galaxies that are unclassified in **VCV** but classified in **SMB**, and vice versa, shown in Table 6. From this sample, we find that 36 of them (80%) are mainly classified as Sy1 while only two are Sy2 with the  $L_{\text{AGN}}^{\text{disc}}$  and machine learning ensemble methods. For the other seven galaxies the classifications are still discrepant. We compare the similarity of the predictions of the  $L_{\text{AGN}}^{\text{disc}}$  and machine learning ensemble methods with the literature. We assume that: i) mixed blazar, BZQ, QSO, NLSy1, Sy1.5 and Sy1.2 galaxies are Type-1 AGN; ii) Sy1.8 are Type-2 AGN; and iii) LINERs cannot be classified as Type-1 nor Type-2 AGN. From galaxies with literature classifications (42 galaxies), we find that more than half of these galaxies (~ 59%) are classified as QSO, and only 11 galaxies (~ 26%) are classified as a Sy1. From the seven galaxies with still discrepant classifications five have other literature classifications. From those five, two galaxies have AGN types similar to those in the literature when  $L_{\text{AGN}}^{\text{disc}}$  is used as a classifier, and only one galaxy when we use machine learning ensemble methods. For the remaining galaxies with literature classifications (37 galaxies), we find that ~ 95% of discrepant galaxies have AGN types similar to those in the literature when both classifiers coincide in the classification.

However, most of the results come from Type-1 AGNs and less than half of these galaxies end up being Seyfert galaxies. The unclassified

**Table 6.** Classification types in discrepant Seyfert galaxies. Columns are similar to Table 5.

Object ID	Classification type			
	$L_{\text{AGN}}^{\text{disc}}$	ML	Literature	Sim.
2E 2294	Sy1	Sy1	QSO	Y
2E 2628	Sy1	Sy1	QSO	Y
2E 3786	Sy1	Sy1	QSO	Y
2MASS J00423990+3017514	Sy1	Sy1	Sy1	Y
2MASS J01341936+0146479	Sy1	Sy1	QSO	Y
2MASS J02500703+0025251	Sy1	Sy1	QSO	Y
2MASS J08171856+5201477	Sy2	Sy1	Sy1	N/Y
2MASS J09393182+5449092	Sy1	Sy1	QSO	Y
2MASS J09455439+4238399	Sy1	Sy1	NLSy1	Y
2MASS J09470326+4640425	Sy1	Sy1	QSO	Y
2MASS J09594856+5942505	Sy1	Sy1	QSO	Y
2MASS J10102753+4132389	Sy1	Sy1	QSO	Y
2MASS J10470514+5444060	Sy1	Sy1	QSO	Y
2MASS J12002696+3317286	Sy1	Sy1	QSO	Y
2MASS J15142051+4244453	Sy1	Sy1	QSO	Y
2MASSI J0930176+470720	Sy1	Sy1	QSO	Y
2MASX J02522087+0043307	Sy1	Sy1	QSO	Y
2MASX J02593816+0042167	Sy1	– <sup>a</sup>	QSO	Y/–
2MASX J06374318-7538458	Sy1	Sy1	Sy1	Y
2MASX J09420770+0228053	Sy1	Sy1	LINER <sup>b</sup>	N
2MASX J09443702-2633554	Sy1	Sy1	Sy1.5 <sup>b</sup>	Y
2MASX J09483841+4030436	Sy2	Sy2	Sy1	N
2MASX J10155660-2002268	Sy1	– <sup>a</sup>	Sy1	Y/–
2MASX J10194946+3322041	Sy1	Sy1	NLSy1	Y
2MASX J15085291+6814074	Sy1	Sy1	Sy1	Y
2MASX J16383091-2055246	– <sup>a</sup>	Sy2	NLSy1	–/N
2MASX J21033788-0455396	Sy1	Sy1	Sy1	Y
2MASX J21512498-0757558	Sy2	Sy2	–	–
2MASX J22024516-1304538	Sy1	Sy1	Sy1	Y
2dFGRS TGN357Z241	Sy1	Sy1	QSO	Y
3C 286	Sy1	Sy1	Mix. blazar	Y
6dFGS gJ034205.4-370322	Sy1	Sy1	Mix. blazar	Y
6dFGS gJ043944.9-454043	Sy1	Sy1	QSO	Y
6dFGS gJ084628.7-121409	Sy1	Sy1	Sy1	Y
CTS 11	Sy1	Sy1	NLSy1	Y
HE 0226-4110	Sy1	Sy1	QSO	Y
ICRF J025937.6+423549	Sy1	Sy1	Mix. blazar	Y
ICRF J081100.6+571412	Sy1	Sy1	QSO	Y
ICRF J100646.4-215920	Sy1	Sy1	Mix. blazar	Y
ICRF J110153.4+624150	Sy1	Sy1	BZQ	Y
ICRF J135704.4+191907	Sy1	Sy1	BZQ	Y
IRAS 10295-1831	Sy1	Sy1	Sy1	Y
Mrk 1361	– <sup>a</sup>	Sy2	–	–
PB 162	– <sup>a</sup>	Sy1	–	–
UGC 10683	Sy2	– <sup>a</sup>	Sy1	N/–

<sup>a</sup> The classification changes depending on the AGN setup used.

<sup>b</sup> Decision based on **VCV**.

and discrepant Seyfert type classifications, presented in Tables 5 and 6, only show part of the predictability potential of these methods but support the usefulness of the classifiers in this work. These results, together with Table 4, show that we can classify AGN types correctly using the physical parameters estimated from broad-band SED fitting using X-CIGALE. In a future study, we expect to use a more complete set of intermediate numerical values for Seyfert galaxies to test their classification.

## 4 DISCUSSIONS

In this section, we further examine the results of this work. First, we discuss the importance of the viewing angle in the AGN SED models (Sect. 4.1) and how they affect current AGN studies (Sect. 4.2). Then, we focus on the AGN types in terms of physical parameters as  $f_{\text{AGN}}$  and SFR (Sect. 4.3), and their classifications (Sect. 4.4). Finally, we examine the effect of not including X-ray data in the SED AGN models (Sect. 4.5).

### 4.1 The role of the viewing angle

In this work, we restricted our results to the seven most important, according to the machine learning techniques, physical parameters when classifying Sy1 and Sy2. Following the AGN unification model, the main difference between these two types of galaxies resides in the viewing angle. Therefore, by comparing these seven parameters, we could understand the role that the viewing angle plays in determining the AGN type.

In Fig. 6, we show how different the AGN setups are when assuming only two viewing angles instead of a full range. With the exception of the viewing angle, all the parameters show a similar behaviour between the different setups. Only small differences in the E(B-V) and observed AGN disc luminosity are observed when comparing SKIRTOR and Fritz setups. Interestingly, in setups with ten viewing angles the estimates give a frequent value of  $\sim 25^\circ$ . Therefore, it seems that the full range of viewing angles in the setup does not significantly affect the other estimated SED parameters.

By construction, the viewing angle in X-CIGALE can determine the AGN type when the angle is close to the face-on ( $0-30^\circ$ ) and edge-on ( $70-90^\circ$ ) scenarios (Yang et al. 2020). Using the Chandra COSMOS Legacy survey (Marchesi et al. 2016) and X-CIGALE, Yang et al. (2020) estimated an accuracy of  $\sim 71\%$  in spectroscopic Type-1 and Type-2 AGNs. In our case, the accuracy of the classifications is around 82-85% when using only the viewing angle (Table 4), although with a different sample size (590 AGNs in Yang et al. (2020) while  $\sim 8000$  in this work). The highest value in the accuracy (and other metrics) is obtained when using a setup with only two angles. If we use a setup with the full range of viewing angles, the distributions for the viewing angle (Fig. 7) are similar to what Gkini et al. (2021) found, where Sy1 are located at values around  $20-30^\circ$  while Sy2 galaxies are more scattered in a wider range of viewing angles. However, the estimations in terms of redshift (Sect. 3.3 and Fig. 9) seems to favour values around  $20-30^\circ$  and  $60-70^\circ$  when looking at Sy1 and Sy2, respectively. Thus, AGNs classifications can be improved by forcing the viewing angle to two values that follow the Type-1 and Type-2 classifications. This result justifies the selection of two or even three viewing angles in similar studies using CIGALE or X-CIGALE in AGN galaxies (e.g. Vika et al. 2017; Zou et al. 2019; Pouliasis et al. 2020; Wang et al. 2020; Mountrichas et al. 2021).

This dichotomy in the viewing angle of AGN SED models could indicate that using the (IR) SED is not an adequate tool to estimate the viewing angle of AGNs as a continuous distribution, compared to spectroscopic measurements of the NLR (Fischer et al. 2013; Marin 2016). In Fig. 5, we show that the viewing angle is not the most important physical parameter when classifying Sy1 and Sy2. The observed AGN disc luminosity has the highest importance score to classify Seyferts, although its UV-optical emission is (in theory) angle-dependent (Netzer 2015; Yang et al. 2020). The power of the observed AGN disc luminosity in separating Sy1 and Sy2 galaxies is stunning when comparing with the viewing angle and other parameters in this work (Figs. 7-9 and Table 4). Using supernovae host

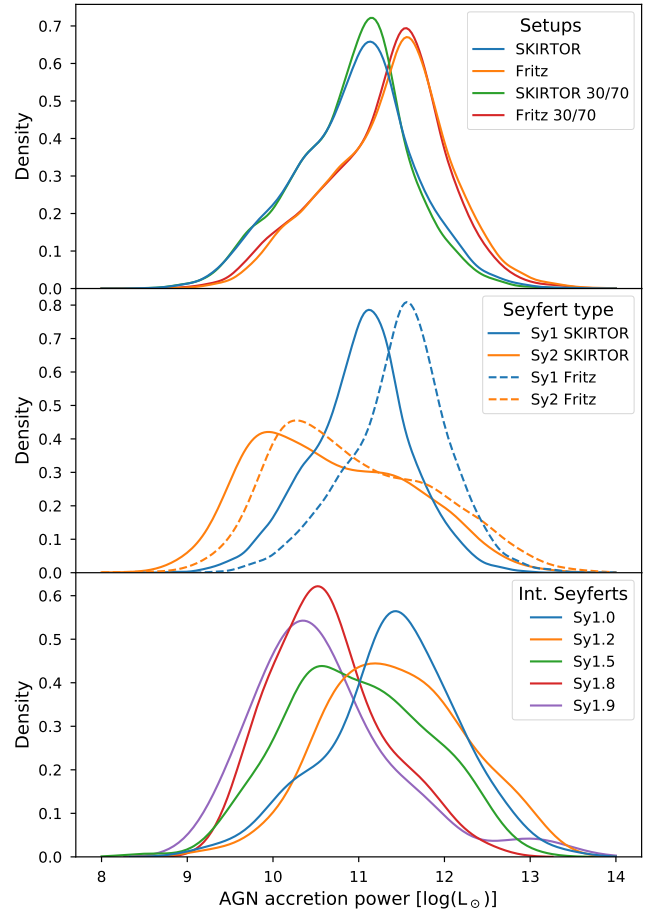


**Figure 10.** Probability density functions for the AGN accretion power of the four AGN setups (upper panel), Seyfert Type-1 and Type-2 for SKIRTOR and Fritz setups (middle panel), and intermediate Seyfert types for the SKIRTOR setup (lower panel). The AGN accretion power (intrinsic disc luminosity) depends on the selected AGN model, but the path from Type-2 to Type-1 AGNs by increasing the AGN accretion power.

galaxies catalogues, Villarroel et al. (2017) shows that the AGN luminosity, together with the stellar age, could play an important role in the AGN unification model beyond the viewing angle estimated from the torus when counting the number of supernovae in Type-2 AGNs. This result is similar to what we find in this work, although the age in the SEDs is not well constrained (Sect. 2.2.3).

In Fig. 10, we verify the estimations of the AGN accretion power for the different Seyfert types and AGN models. We notice that Fritz setups estimate higher accretion powers than SKIRTOR setups. This result is due to a different anisotropy correction applied in X-CIGALE, where the AGN accretion power does not depend on the viewing angle for the Fritz models. As a result of this correction, the difference between Seyfert types (middle panel) have different accretion powers depending on the AGN model. Therefore,  $L_{\text{AGN}}^{\text{disc}}$  cannot be easily transformed into bolometric luminosities due to its complex dependencies on the models. However, when we use only one of the AGN models in the intermediate Seyfert types, we notice similar distributions as with the  $L_{\text{AGN}}^{\text{disc}}$ . Therefore, the more detailed spectroscopic classifications follow a path from Type-2 to Type-1 AGNs by increasing the observed and intrinsic AGN disc luminosity (Sect. 3.2.3 and Figs. 8 and 10). This means that the AGN disc

luminosity is an important factor, if not the main, in deciphering AGN types with SED models, and that a probable evolutionary path from intermediate types can be obtained with the AGN disc luminosity (Elitzur et al. 2014).

This result could have an impact in cosmological estimations done in AGNs. For example, QSOs are used to measure the luminosity distance at high redshifts to determine cosmological parameters (e.g. Lusso et al. 2019). If there is a dependency in the luminosity distance of QSOs with the viewing angle, it would lead to incorrect cosmological estimates (Prince et al. 2021). Even if the dependency is not entirely on the viewing angle but on the brightness of the AGN, then these estimates should be reformulated.

#### 4.2 The AGN dust winds

As we mentioned before, X-CIGALE follows the simple AGN-unification scheme, i.e. the viewing angle determines the AGN type (Yang et al. 2020). If this simplified scheme is correct, the viewing angle should be the best classifier in our sample, but it is not. Our results for the smooth and clumpy torus models (Fritz and SKIRTOR, respectively) show that the observed AGN disc luminosity is a better classifier than the viewing angle. Perhaps the AGN “zoo” of galaxies is too complex to be explained with only the angle-dependent obscuration coming from a toroidal structure (Padovani et al. 2017).

A possible solution is the AGN disc-wind scenario (Emmering et al. 1992; Elitzur & Shlosman 2006; Netzer 2015). For example, Hönic & Kishimoto (2017) propose a model where dusty winds can explain the observational results on spatially resolved AGNs (e.g. García-Burillo et al. 2021; Alonso-Herrero et al. 2021). Later on, this model was extended by Hönic (2019), following interferometry IR and sub-mm observations (e.g. López-Gonzaga et al. 2016) where the AGN structure is composed of disc, wind and wind launching regions instead of a simple toroidal obscuration structure. In this scenario, the multiphase structure is consistent with the relation between the AGN obscured fraction (covering fraction) and AGN luminosity (Eddington ratio) in X-rays (Merloni et al. 2014; Ricci et al. 2017). The winds provide additional obscuration traced by covering factors and could separate the obscured and unobscured regions, and thus separate Type-1 and Type-2 AGNs. Similarly, Ogawa et al. (2021) describe a disc wind model analogous to Hönic (2019) using X-CLUMPY (Nenkova et al. 2008; Tanimoto et al. 2019), another SED toroidal model. In that work, X-CLUMPY is used in two different models for obscured and unobscured AGNs. With this approach, Ogawa et al. (2021) also finds a negative correlation between the Eddington ratio and the torus covering factor. Therefore, it is possible that the estimates of the AGN disc luminosity can be affected by other structures, like the ones proposed by Hönic (2019) or Ogawa et al. (2021). These structures may explain why the estimated observed AGN disc luminosity works better as a classifier in Sy1 and Sy2 with X-CIGALE.

An advantage of dusty wind structures is that they can also explain the origin of the red QSOs. These red QSOs are expected to be red due to dust in the line of sight (Webster et al. 1995), although it has recently been proposed that it is related to an evolutionary phase of QSO (Klindt et al. 2019). Calistro Rivera et al. (2021) studied the nature of red QSO using AGN<sub>FITTER</sub> (Calistro Rivera et al. 2016), which resides in SED templates of smooth toroidal models (Silva et al. 2004), and found no connection between the AGN torus and the QSO reddening. However, they also found high-velocity winds in these red QSOs, suggesting that dusty wind structures may explain their nature.

Interestingly, even the intermediate Seyfert types can be explained

with the disc-wind scenario. Elitzur et al. (2014) show that an evolutionary path of intermediate Seyfert types is related to the wind streamlines. When the accretion rate decreases the AGN luminosity decreases because the clouds in the wind streamlines move from high to low altitudes, generating an evolution sequence from 1.0 to 1.9 AGN types. This path is similar to the one presented in Sect. 3.2.3 and Figs. 8 and 10, where AGN disc luminosity decreases with Seyfert type. The estimations presented in this work support this idea, as the mean AGN accretion power is lower in Sy2 galaxies by  $\sim 0.5$  dex than in Sy1 galaxies. However, we need to keep in mind that: i) the estimates of the physical parameters coming from AGN SED models depend on the chosen model (as shown in Fig. 10 and by González-Martín et al. 2019a,b), and ii) the classification criteria for the intermediate types are different in Elitzur et al. (2014) and this work. Therefore, we need more information in terms of intermediate type classifications and in-depth observations of AGN regions with multi-wavelength observations to create a robust connection between theoretical models and observations.

#### 4.3 AGN fraction and SFR in AGN types

To describe the difference between Type-1 and Type-2 AGN other physical parameters could be used besides AGN luminosity and viewing angle. In Sect. 3.2.2 and Fig. 7, we mentioned that parameters like  $f_{\text{AGN}}$  and SFR can also differentiate Seyfert types. However, we argue that the differences between AGN types will be smaller in these physical parameters.

In terms of the AGN contribution to the total IR luminosity ( $f_{\text{AGN}}$ ), Gruppioni et al. (2016) found that Sy2 galaxies tend to have a lower  $f_{\text{AGN}}$  compared with Sy1, in a sample of local galaxies. Similar results are found by Ramos Padilla et al. (2020), where six Type-1 AGN galaxies have higher  $f_{\text{AGN}}$  than AGN types with an estimated viewing angle of  $60^\circ$ , generally Type-2 AGNs. They also found that the  $f_{\text{AGN}}$  could increase with IR luminosity, as Alonso-Herrero et al. (2012) suggested. Therefore, Sy1 could have a higher AGN fraction than Sy2 because of their higher IR luminosity (e.g. Suh et al. 2019, and references therein). We find a similar behaviour in Fig. 7, although the values are widely distributed between both types. In addition, in Fig. 9, we find a slight increase of  $f_{\text{AGN}}$  with redshift as found by other works (e.g. Wang et al. 2020), especially in Sy2 galaxies, but the statistic is small. The discrepancy in the results may also lie in the selection effects when comparing AGN types of galaxies, due to sample selection (e.g. Calistro Rivera et al. 2016), AGN definitions (e.g. Wang et al. 2020), or incorrect estimates of  $f_{\text{AGN}}$  because of cold-dust emission (McKinney et al. 2021). Therefore, it is not yet clear how  $f_{\text{AGN}}$ , or its relationship to total IR luminosity, will change at higher redshifts ( $z > 1$ ) between AGN types.

For the SFR, the relative importance is small when separating the two Seyfert types, following the feature selection (Sect. 3.1). This result agrees with Suh et al. (2019) and Masoura et al. (2021), who found no differences between AGN types in terms of SFR and stellar mass associated with AGN power in X-rays, although large uncertainties are present for Type-1 AGNs. On the other hand, Zou et al. (2019) show differences in stellar mass but not in SFR between AGN types, even using different SFR calculation methods (SED,  $H_\alpha$  and IR luminosities). In this work, stellar mass is estimated with X-CIGALE but its relative importance is even lower than the importance of the SFR. In addition, we do not find a clear separation between the two Seyfert types in terms of SFR with redshift (Fig. 9). The SFR will increase for both types as the SFR increases with the redshift until the cosmic noon, therefore we are only seeing a selection effect.

Thus, looking at  $f_{\text{AGN}}$  and SFR individually may give some clues

about the difference between AGN types. However, the differences are small when compared together with other physical parameters, such as the observed AGN disc luminosity. Furthermore, one of the main problems of looking at different physical parameters resides in the definition between obscured (Type-2) and unobscured (Type-1) AGNs (Hickox & Alexander 2018), as we will see in the following subsection.

#### 4.4 AGN Classifications

In this work, we treated the Seyfert types coming from SMB and VCV as true classifications. However, that does not mean that the Seyfert galaxy sample studied here is not populated with other types of AGN galaxies. For example, galaxies that we assume as unclassified Seyfert end up being mostly QSO in the literature (Sect. 3.5). In any case, we have presented evidence from different AGN setups that seem to agree with the general classification of Type-1 and Type-2 AGN. Then, we could use simple relations, like the one presented in Eq. 3, to separate AGN galaxies using the features estimated from SED modelling of the AGN component available in X-CIGALE. Machine learning ensemble techniques could also be used to classify galaxies with X-CIGALE outputs, achieving even higher accuracy than just one physical parameter (Table 4). Nevertheless, these methods will require correct classifications of galaxies that sometimes are not available.

As we discussed in Sect. 4.2, the intermediate Seyfert classifications could help solve the problems of the AGN unification model. If these galaxies are an evolutionary stage of AGNs, as proposed by Elitzur et al. (2014) with disc wind models, then classifying AGN galaxies could be crucial to join the theoretical models with observations. In this work, all the intermediate classifications come from VCV with the quantitative approach of Winkler (1992), as described in Sect. 3.2.3. However, other criteria could be applied in the classification of intermediate AGN galaxies (e.g. Stern & Laor 2012). More spectral information and consistent classifications will be needed in intermediate AGN galaxies to clarify this evolutionary stage, for example using the on-going DEVILS survey. Future observations with the *James Webb Space Telescope* (JWST) will detect obscured AGNs and calculate AGN fractional contributions through photometry and spectral line features (e.g. Satyapal et al. 2021; Yang et al. 2021), which will elucidate the path for classifying these type of galaxies.

#### 4.5 X-ray information

The efforts to create catalogues of AGN galaxies with X-ray data are crucial to classify galaxies missed in optical catalogues (e.g. Koss et al. 2017). These missed galaxies are in general obscured AGN galaxies (Type-2), which are difficult to classify, even using ensemble methods in optical wavelengths (Golob et al. 2021). However, it is good to keep in mind that Type-2 AGNs could remain undetected in IR and X-ray colour surveys (Pouliasis et al. 2020). Therefore, a multi-wavelength study, like the one presented in this work, is ideal to tackle the completeness and classification problem in AGN galaxies.

Unfortunately, a limitation of this study is the lack of X-ray data when fitting the SED, although there is a correlation between the AGN MIR luminosity and the 2–10 keV X-ray luminosity in Type-1 and Type-2 AGNs (Gandhi et al. 2009; Suh et al. 2019). We conclude that the quantity of photometric data in NED and CDS is not enough nor homogeneous to include the X-ray module in the X-CIGALE setups. None the less, X-rays can help to constrain non-physical parameters in SED tools as X-CIGALE (Yang et al. 2020). Recent

studies with different SEDs models that include X-ray data show how important the inclusion of these data could be to constrain the AGN models (e.g. Suh et al. 2019; Ogawa et al. 2021; Mountrichas et al. 2021; Masoura et al. 2021). In the future, we expect to understand the probable evolutionary paths discussed in this work for different AGN types, with the AGN luminosity,  $f_{\text{AGN}}$ , and X-ray data. In the next decade, the combination of the *Athena space telescope* with X-CIGALE will help to unambiguously determine the presence of AGN for this type of works (Yang et al. 2020).

## 5 CONCLUSIONS

We have used a sample of 13 173 Seyfert galaxies from SMB and VCV to assess the importance of the viewing angle in AGN SED models. We have used a data-driven approach by retrieving photometric data from astronomical databases (CDS and NED) to be used in the SED analysis with X-CIGALE. Two AGN SED toroidal models (Fritz and SKIRTOR setups) were used with different viewing angle configurations to verify the effect of viewing angle selection in the estimated physical parameters. These estimates have been validated by comparing our results with those from Vika et al. (2017), showing good agreement except for the AGN fractions, which can be related to the different assumptions of the grids.

Our main conclusions are the following:

1. The estimated viewing angle from X-CIGALE seems to be the second best discriminator when assessing AGN type. This result is supported by different prediction metrics and importance scores in machine learning algorithms which favour the observed AGN disc luminosity as the most important physical parameter.
2. The initial viewing angle assumption in X-CIGALE does not significantly affect the other estimated physical parameters if at least two viewing angles that follow the AGN Type-1 and Type-2 classifications are taken into account.
3. At different redshifts ( $z \lesssim 0.5$ ), the smooth and clumpy torus AGN models seem to favour viewing angles around 20–30° and 60–70° when looking at Sy1 (Type-1 AGN) and Sy2 (Type-2 AGN), respectively. While in terms of the observed AGN disc luminosity, we propose to use a limit (Eq. 3) that separates both types. These values may predict the AGN type in unclassified AGN galaxies, as shown in the case of unclassified and discrepant Seyfert galaxies.
4. Machine learning ensemble methods can be used for AGN classification tasks but require the use of several parameters from X-CIGALE. These parameters include individual physical parameters that are important for the classification (e.g. viewing angle or observed AGN disc luminosity). Nevertheless, these methods require correct classifications (training data) that often vary based on criteria.
5. The observed and intrinsic AGN disc luminosity decreases from Type-1 to Type-2 AGNs in the intermediate Seyfert types. This decrease may be explained by accretion rates within AGN disc wind models, which show an evolutionary path among these AGN types. However, more information is needed to create a robust connection between theoretical models and observations.

In this work, we have demonstrated usefulness of the broad-band SED tool as X-CIGALE to classify AGN galaxies in Type-1 and Type-2. Thus, X-CIGALE could be a powerful tool to characterise AGNs in the upcoming years. Future space telescopes like the JWST and *Athena* will get crucial photometry and spectroscopy to constrain AGN physical parameters like luminosity and  $f_{\text{AGN}}$ , which will improve AGN galaxy classifications. These classifications along with

other physical parameters will help us understand the real scenario that describes AGN galaxies.

## ACKNOWLEDGEMENTS

K. Małek has been supported by the Polish National Science Centre grant (UMO-2018/30/E/ST9/00082). We would like to thank the Center for Information Technology of the University of Groningen for their support and for providing access to the Peregrine high performance computing cluster. We acknowledge the anonymous referee for a careful reading of the manuscript and very helpful suggestions and comments.

This research made use of Astropy,<sup>5</sup> a community-developed core Python package for Astronomy (Astropy Collaboration et al. 2013, 2018). This research has made use of the SIMBAD database, operated at CDS, Strasbourg, France. This research has made use of the NASA/IPAC Extragalactic Database (NED), which is funded by the National Aeronautics and Space Administration and operated by the California Institute of Technology. This research has made use of NASA's Astrophysics Data System Bibliographic Services. Part of the initial exploratory analysis was performed with TOPCAT (Taylor 2005).

## DATA AVAILABILITY

Most of the data and code underlying this article are available in Zenodo, at <https://doi.org/10.5281/zenodo.5227294>. The X-CIGALE estimated data from the AGN setups are available in a companion repository in Zenodo, at <https://doi.org/10.5281/zenodo.5221764>, which also includes a script to create similar figures like the one presented in Fig. 2 for all galaxies in this work.

## REFERENCES

- Abazajian K. N., et al., 2009, *ApJS*, **182**, 543
- Ai Y. L., et al., 2016, *AJ*, **151**, 24
- Albaret F. D., et al., 2015, *MNRAS*, **452**, 4153
- Alonso-Herrero A., Pereira-Santaella M., Rieke G. H., Rigopoulou D., 2012, *ApJ*, **744**, 2
- Alonso-Herrero A., et al., 2021, *A&A*, **652**, A99
- Antonucci R., 1993, *ARA&A*, **31**, 473
- Antonucci R. R. J., Miller J. S., 1985, *ApJ*, **297**, 621
- Astropy Collaboration et al., 2013, *A&A*, **558**, A33
- Astropy Collaboration et al., 2018, *AJ*, **156**, 123
- Baqui P. O., et al., 2021, *A&A*, **645**, A87
- Bernhard E., Tadhunter C., Mullaney J. R., Grimmett L. P., Rosario D. J., Alexander D. M., 2021, *MNRAS*, **503**, 2598
- Bluck A. F. L., Maiolino R., Sánchez S. F., Ellison S. L., Thorp M. D., Piotrowska J. M., Teimoorinia H., Bundy K. A., 2020, *MNRAS*, **492**, 96
- Boquien M., Burgarella D., Roehly Y., Buat V., Ciesla L., Corre D., Inoue A. K., Salas H., 2019, *A&A*, **622**, A103
- Braatz J. A., Wilson A. S., Gezari D. Y., Varosi F., Beichman C. A., 1993, *ApJ*, **409**, L5
- Breiman L., 2001, *Machine Learning*, **45**, 5
- Brunet C., et al., 2018, in European Physical Journal Web of Conferences. p. 02004, doi:10.1051/epjconf/201818602004
- Bruzual G., Charlot S., 2003, *MNRAS*, **344**, 1000
- Buat V., Ciesla L., Boquien M., Małek K., Burgarella D., 2019, *A&A*, **632**, A79
- Buat V., et al., 2021, *A&A*, **654**, A93
- Burgarella D., Buat V., Iglesias-Páramo J., 2005, *MNRAS*, **360**, 1413
- Calistro Rivera G., Lusso E., Hennawi J. F., Hogg D. W., 2016, *ApJ*, **833**, 98
- Calistro Rivera G., et al., 2021, *A&A*, **649**, A102
- Calzetti D., Armus L., Bohlin R. C., Kinney A. L., Koornneef J., Storchi-Bergmann T., 2000, *ApJ*, **533**, 682
- Cameron M., Storey J. W. V., Rotaciuc V., Genzel R., Verstraete L., Drapatz S., Siebenmorgen R., Lee T. J., 1993, *ApJ*, **419**, 136
- Carleo G., Cirac I., Cranmer K., Daudet L., Schuld M., Tishby N., Vogt-Maranto L., Zdeborová L., 2019, *Reviews of Modern Physics*, **91**, 045002
- Casey C. M., 2012, *MNRAS*, **425**, 3094
- Chabrier G., 2003, *PASP*, **115**, 763
- Chen T., Guestrin C., 2016, arXiv e-prints, p. arXiv:1603.02754
- Chen S., et al., 2018, *A&A*, **615**, A167
- Ciesla L., et al., 2015, *A&A*, **576**, A10
- Ciesla L., Elbaz D., Schreiber C., Daddi E., Wang T., 2018, *A&A*, **615**, A61
- Cusumano G., et al., 2010, *A&A*, **524**, A64
- D'Abrusco R., Massaro F., Paggi A., Smith H. A., Masetti N., Landoni M., Tosti G., 2014, *ApJS*, **215**, 14
- D'Abrusco R., et al., 2019, *ApJS*, **242**, 4
- Dale D. A., Helou G., Magdis G. E., Armus L., Díaz-Santos T., Shi Y., 2014, *ApJ*, **784**, 83
- Dietrich J., et al., 2018, *MNRAS*, **480**, 3562
- Dong X. Y., et al., 2018, *AJ*, **155**, 189
- Duarte Puertas S., Vilchez J. M., Iglesias-Páramo J., Kehrig C., Pérez-Montero E., Rosales-Ortega F. F., 2017, *A&A*, **599**, A71
- Dullemond C. P., van Bemmell I. M., 2005, *A&A*, **436**, 47
- Efstathiou A., 2006, *MNRAS*, **371**, L70
- Efstathiou A., Rowan-Robinson M., 1995, *MNRAS*, **273**, 649
- Efstathiou A., Hough J. H., Young S., 1995, *MNRAS*, **277**, 1134
- Elitzur M., Shlosman I., 2006, *ApJ*, **648**, L101
- Elitzur M., Ho L. C., Trump J. R., 2014, *MNRAS*, **438**, 3340
- Emmering R. T., Blandford R. D., Shlosman I., 1992, *ApJ*, **385**, 460
- Fabian A. C., Vasudevan R. V., Gandhi P., 2008, *MNRAS*, **385**, L43
- Fischer T. C., Crenshaw D. M., Kraemer S. B., Schmitt H. R., 2013, *ApJS*, **209**, 1
- Flesch E. W., 2015, *Publ. Astron. Soc. Australia*, **32**, e010
- Flesch E. W., 2021, *VizieR Online Data Catalog*, p. VII/290
- Florez J., et al., 2020, *MNRAS*, **497**, 3273
- Friedman J. H., 2001, *Annals of statistics*, pp 1189–1232
- Fritz J., Franceschini A., Hatziminaoglou E., 2006, *MNRAS*, **366**, 767
- Gandhi P., Horst H., Smette A., Hönig S., Comastri A., Gilli R., Vignali C., Duschl W., 2009, *A&A*, **502**, 457
- García-Burillo S., et al., 2021, *A&A*, **652**, A98
- Gentile Fusillo N. P., Gänsicke B. T., Greiss S., 2015, *MNRAS*, **448**, 2260
- Gkini A., Plionis M., Chira M., Koulouridis E., 2021, *A&A*, **650**, A75
- Golob A., Sawicki M., Goulding A. D., Coupon J., 2021, *MNRAS*, **503**, 4136
- González-Martín O., et al., 2019a, *ApJ*, **884**, 10
- González-Martín O., et al., 2019b, *ApJ*, **884**, 11
- Granato G. L., Danese L., 1994, *MNRAS*, **268**, 235
- Gruppioni C., et al., 2016, *MNRAS*, **458**, 4297
- Gupta M., Sikora M., Nalewajko K., 2016, *MNRAS*, **461**, 2346
- Hickox R. C., Alexander D. M., 2018, *ARA&A*, **56**, 625
- Hönig S. F., 2019, *ApJ*, **884**, 171
- Hönig S. F., Kishimoto M., 2017, *ApJ*, **838**, L20
- Järvälä E., Lähteenmäki A., León-Tavares J., 2015, *A&A*, **573**, A76
- Jayasinghe T., et al., 2018, *MNRAS*, **477**, 3145
- Kass R. E., Raftery A. E., 1995, *Journal of the American Statistical Association*, **90**, 773
- Kauffmann G., et al., 2003, *MNRAS*, **346**, 1055
- Klindt L., Alexander D. M., Rosario D. J., Lusso E., Fotopoulou S., 2019, *MNRAS*, **488**, 3109
- Koss M., et al., 2017, *ApJ*, **850**, 74
- Krawczyk C. M., Richards G. T., Mehta S. S., Vogeley M. S., Gallagher S. C., Leighly K. M., Ross N. P., Schneider D. P., 2013, *ApJS*, **206**, 4
- Krawczyk C. M., Richards G. T., Gallagher S. C., Leighly K. M., Hewett P. C., Ross N. P., Hall P. B., 2015, *AJ*, **149**, 203
- Krolik J. H., Begelman M. C., 1988, *ApJ*, **329**, 702

<sup>5</sup> <http://www.astropy.org>

- LaMassa S. M., et al., 2015, *ApJ*, **800**, 144
- Lebouteiller V., Barry D. J., Goes C., Sloan G. C., Spoon H. W. W., Weedman D. W., Bernard-Salas J., Houck J. R., 2015, *ApJS*, **218**, 21
- Leja J., Johnson B. D., Conroy C., van Dokkum P., 2018, *ApJ*, **854**, 62
- Liu H.-Y., Yuan W., Dong X.-B., Zhou H., Liu W.-J., 2018, *ApJS*, **235**, 40
- López-Gonzaga N., Bartscher L., Tristram K. R. W., Meisenheimer K., Schartmann M., 2016, *A&A*, **591**, A47
- Lusso E., Piedipalumbo E., Risaliti G., Paolillo M., Bisogni S., Nardini E., Amati L., 2019, *A&A*, **628**, L4
- Lyu J., Rieke G. H., 2018, *ApJ*, **866**, 92
- Małek K., et al., 2018, *A&A*, **620**, A50
- Marchesi S., et al., 2016, *ApJ*, **817**, 34
- Marin F., 2016, *MNRAS*, **460**, 3679
- Masoura V. A., Mountrichas G., Georgantopoulos I., Plionis M., 2021, *A&A*, **646**, A167
- Matthews B. W., 1975, *Biochimica et Biophysica Acta (BBA)-Protein Structure*, **405**, 442
- McKinney J., Hayward C. C., Rosenthal L. J., Martínez-Galarza J. R., Pope A., Sajina A., Smith H. A., 2021, arXiv e-prints, p. arXiv:2103.12747
- Merloni A., et al., 2014, *MNRAS*, **437**, 3550
- Meusinger H., Hinze A., de Hoon A., 2011, *A&A*, **525**, A37
- Miettinen O., 2018, *Ap&SS*, **363**, 197
- Mountrichas G., Buat V., Yang G., Boquien M., Burgarella D., Ciesla L., 2021, *A&A*, **646**, A29
- Mullaney J. R., Alexander D. M., Goulding A. D., Hickox R. C., 2011, *MNRAS*, **414**, 1082
- Neškova M., Ivezić Ž., Elitzur M., 2002, *ApJ*, **570**, L9
- Neškova M., Sirocky M. M., Nikutta R., Ivezić Ž., Elitzur M., 2008, *ApJ*, **685**, 160
- Netzer H., 2015, *ARA&A*, **53**, 365
- Noll S., Burgarella D., Giovannoli E., Buat V., Marcillac D., Muñoz-Mateos J. C., 2009, *A&A*, **507**, 1793
- Oberto A., et al., 2020, in Ballester P., Ibsen J., Solar M., Shorridge K., eds, *Astronomical Society of the Pacific Conference Series Vol. 522, Astronomical Data Analysis Software and Systems XXVII*. p. 105
- Ogawa S., Ueda Y., Tanimoto A., Yamada S., 2021, *ApJ*, **906**, 84
- Oh K., Yi S. K., Schawinski K., Koss M., Trakhtenbrot B., Soto K., 2015, *ApJS*, **219**, 1
- Osterbrock D. E., 1977, *ApJ*, **215**, 733
- Osterbrock D. E., 1981, *ApJ*, **249**, 462
- Osterbrock D. E., Pogge R. W., 1985, *ApJ*, **297**, 166
- Padovani P., et al., 2017, *A&ARv*, **25**, 2
- Panessa F., Castangia P., Malizia A., Bassani L., Tarchi A., Bazzano A., Ubertini P., 2020, *A&A*, **641**, A162
- Pâris I., et al., 2018, *A&A*, **613**, A51
- Pedregosa F., et al., 2012, arXiv e-prints, p. arXiv:1201.0490
- Pérez-Torres M., Mattila S., Alonso-Herrero A., Aalto S., Efstathiou A., 2021, *A&ARv*, **29**, 2
- Pier E. A., Krolik J. H., 1992, *ApJ*, **401**, 99
- Pouliasis E., Mountrichas G., Georgantopoulos I., Ruiz A., Yang M., Bonanos A. Z., 2020, *MNRAS*, **495**, 1853
- Prevot M. L., Lequeux J., Maurice E., Prevot L., Rocca-Volmerange B., 1984, *A&A*, **132**, 389
- Prince R., Czerny B., Pollo A., 2021, *ApJ*, **909**, 58
- Rakshit S., Stalin C. S., Chand H., Zhang X.-G., 2017, *ApJS*, **229**, 39
- Ramos Almeida C., Ricci C., 2017, *Nature Astronomy*, **1**, 679
- Ramos Padilla A. F., Ashby M. L. N., Smith H. A., Martínez-Galarza J. R., Beverage A. G., Dietrich J., Higuera-G. M.-A., Weiner A. S., 2020, *MNRAS*, **499**, 4325
- Ricci C., et al., 2017, *Nature*, **549**, 488
- Salmon B., et al., 2016, *ApJ*, **827**, 20
- Salpeter E. E., 1955, *ApJ*, **121**, 161
- Satyapal S., Kamal L., Cann J. M., Secrest N. J., Abel N. P., 2021, *ApJ*, **906**, 35
- Schmidt E. O., Ferreira D., Vega Neme L., Oio G. A., 2016, *A&A*, **596**, A95
- Scott D. W., 2015, *Multivariate Density Estimation: Theory, Practice, and Visualization*
- Scott A. E., Stewart G. C., 2014, *MNRAS*, **438**, 2253
- Serra P., Amblard A., Temi P., Burgarella D., Giovannoli E., Buat V., Noll S., Im S., 2011, *ApJ*, **740**, 22
- Siebenmorgen R., Heymann F., Efstathiou A., 2015, *A&A*, **583**, A120
- Silva L., Maiolino R., Granato G. L., 2004, *MNRAS*, **355**, 973
- Souchay J., et al., 2015, *A&A*, **583**, A75
- Stalevski M., Fritz J., Baes M., Nakos T., Popović L. Č., 2012, *MNRAS*, **420**, 2756
- Stalevski M., Ricci C., Ueda Y., Lira P., Fritz J., Baes M., 2016, *MNRAS*, **458**, 2288
- Stern J., Laor A., 2012, *MNRAS*, **426**, 2703
- Suh H., et al., 2019, *ApJ*, **872**, 168
- Sun J., Shen Y., 2015, *ApJ*, **804**, L15
- Tamayo D., et al., 2016, *ApJ*, **832**, L22
- Tanimoto A., Ueda Y., Odaka H., Kawaguchi T., Fukazawa Y., Kawamuro T., 2019, *ApJ*, **877**, 95
- Taylor M. B., 2005, in Shopbell P., Britton M., Ebert R., eds, *Astronomical Society of the Pacific Conference Series Vol. 347, Astronomical Data Analysis Software and Systems XIV*. p. 29
- Tharwat A., 2020, *Applied Computing and Informatics*
- Thorne J. E., et al., 2021, *MNRAS*, **505**, 540
- Toba Y., et al., 2014, *ApJ*, **788**, 45
- Toba Y., et al., 2021, *ApJ*, **912**, 91
- Urry C. M., Padovani P., 1995, *PASP*, **107**, 803
- Véron-Cetty M. P., Véron P., 2010, *A&A*, **518**, A10
- Vika M., Ciesla L., Charmandaris V., Xilouris E. M., Lebouteiller V., 2017, *A&A*, **597**, A51
- Villarroel B., Nyholm A., Karlsson T., Comerón S., Korn A. J., Sollerman J., Zackrisson E., 2017, *ApJ*, **837**, 110
- Virtanen P., et al., 2020, *Nature Methods*, **17**, 261
- Wada K., 2015, *ApJ*, **812**, 82
- Wang T.-W., et al., 2020, *MNRAS*, **499**, 4068
- Webster R. L., Francis P. J., Petersont B. A., Drinkwater M. J., Masci F. J., 1995, *Nature*, **375**, 469
- Wenger M., et al., 2000, *A&AS*, **143**, 9
- Winkler H., 1992, *MNRAS*, **257**, 677
- Yang G., et al., 2020, *MNRAS*, **491**, 740
- Yang G., et al., 2021, *ApJ*, **908**, 144
- Zhou H., Wang T., Yuan W., Lu H., Dong X., Wang J., Lu Y., 2006, *ApJS*, **166**, 128
- Zou F., Yang G., Brandt W. N., Xue Y., 2019, *ApJ*, **878**, 11

## APPENDIX A: NARROW-LINE SY1 GALAXIES

The narrow-line Sy1 (NLSy1) are AGN galaxies that share similarities with Sy1 and Sy2, but cannot be identified as an intermediate Seyfert type (Osterbrock & Pogge 1985). These galaxies are classified as NLSy1 due to their i) H $\beta$  line emission profile (broad and narrow components), ii) ratio between H $\beta$  and [O III] fluxes below 3 ( $R < 3$ ), iii) narrow FWHM, and iv) the presence of [Fe II] multiplets (e.g. Zhou et al. 2006; Rakshit et al. 2017; Chen et al. 2018). These characteristics indicate that NLSy1 are similar to Sy1. None the less, NLSy1 seem to show higher Eddington rates, lower black hole masses and different viewing angles (Rakshit et al. 2017).

We assumed that NLSy1 are Sy1 galaxies in the catalogue of VCV, as most of these NLSy1 were classified as Sy1 in SMB. However, the results from the AGN setups in this work show small differences in the AGN parameters between these two AGN types. In Figure A1, we present the density functions of the AGN physical parameters for NLSy1 and Sy1 as classified by VCV. For almost all physical parameters the median values for these AGN types are different, although it does not show any difference for the viewing angle. The null hypothesis of the KS test is always rejected when comparing NLSy1 and Sy1 galaxies. All the parameters have a higher  $D$  value than the critical value,  $D_{\text{crit}} = 0.04$  in the SKIRTOR setup. This means that

both samples originate from different distributions. Nevertheless, in terms of the viewing angle, we notice the smallest difference between these two types ( $D = 0.08$ ). This small difference supports our assumption that Sy1 and NLSy1 can be treated as the same type in this work, as our focus resides in the AGN viewing angle.

Conversely, there are larger differences in the total AGN luminosity, as well in terms of their components (disc and re-emitted dust) and intrinsic accretion power ( $D > 0.24$ ). These differences may be related to the higher accretion of the AGN in this type of galaxy. Nevertheless, the difference in the AGN physical parameters for Sy1 and NLSy1 may require the X-ray bands, which were not obtained in this work (Sect. 4.5), as they seem to show a steeper X-ray slope in NLSy1 (Scott & Stewart 2014). Then, a more specific study of these two types of galaxies will be required to understand their nature.

## APPENDIX B: MOCK RESULTS

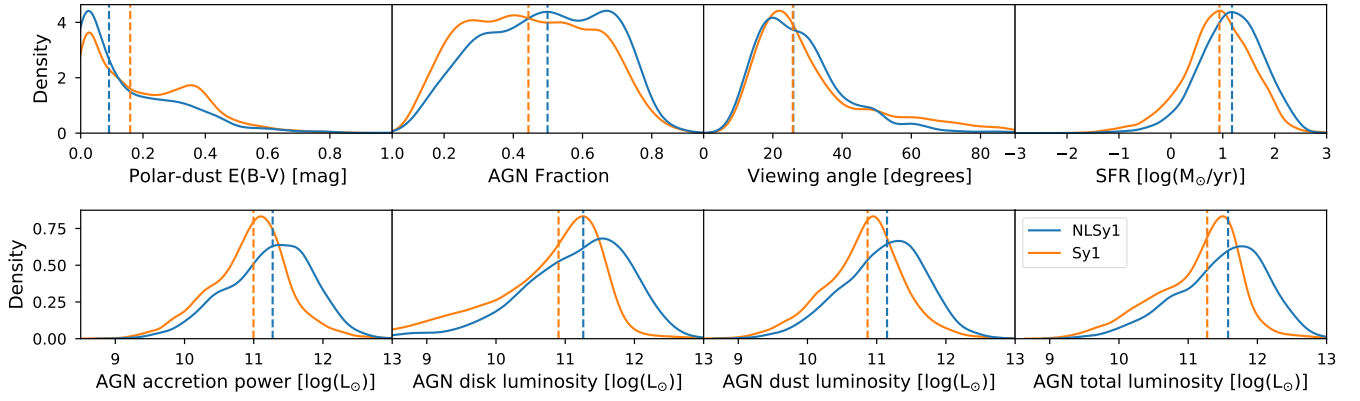
We perform a mock analysis on the main physical parameters to verify the quality of the fits inside X-CIGALE. We use the estimations from the SKIRTOR and Fritz setups. The mock analysis is performed inside X-CIGALE by creating mock values from the original photometry flux and errors and the best fit of the object. Then, the same method used in the original estimation is applied to obtain mock estimations. With this analysis, we can estimate the reliability of the obtained estimations for the physical parameters (Boquien et al. 2019; Yang et al. 2020).

Figure B1 shows the mock analysis for the SKIRTOR setup in the seven selected parameters used for this study (Sect. 3.1) with the addition of the accretion power (intrinsic disc luminosity) and stellar mass. In general, all the physical parameters are well correlated, although some parameters tend to have larger uncertainties such as polar dust and viewing angle. The e-folding time of the main stellar population ( $\tau_{\text{main}}$ ) is the most affected parameter when comparing with mock values. This result is expected as the age estimates inside CIGALE are not well constrained, as noted by Vika et al. (2017) and shown in Sect. 2.2.3. The mock analysis for the Fritz setup (found in the online repository) shows similar results as the Fritz setup. Therefore, the quality of the fits allows us to analyse the estimated physical parameters in this work.

## APPENDIX C: CLASSIFICATIONS OF INDIVIDUAL OBJECTS IN THE LITERATURE

For the 14 unclassified and 45 discrepant Seyfert classifications discussed in Sect. 3.5, we searched the literature for other classifications of activity type. In Table C1, we present the activity type information and the reference for these classifications. We did not find another classification for some of these galaxies, therefore these galaxies are not listed in Table C1.

This paper has been typeset from a TeX/LaTeX file prepared by the author.



**Figure A1.** Probability density functions for the AGN estimated parameters and SFR comparing NLSy1 (blue) and Sy1 (orange) galaxies for the SKIRTOR setup with the respective median values (vertical dashed lines). No difference is observed in the viewing angle median estimates. However, NLSy1 show a higher luminosity in the intrinsic component (accretion power), the emitted disc, dust luminosities and the total AGN luminosity.

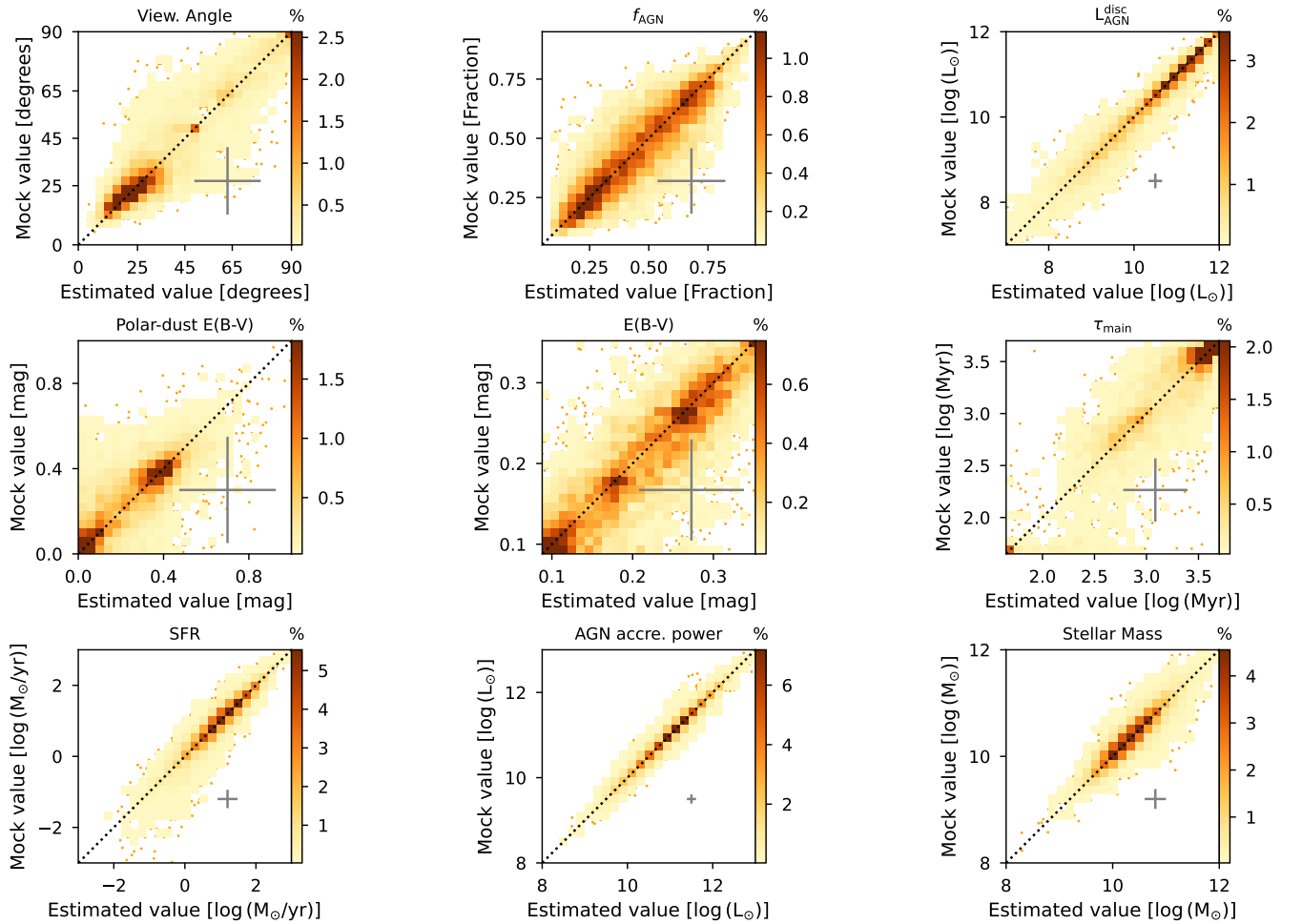


**Figure B1.** Mock versus estimated values from SKIRTOR setup for nine parameters studied in this work. The 2-dimensional histograms show the percentage of galaxies in the sample that fall in the parameter space sampled by 25 cells in each dimension. The pointed line represents the 1:1 relation and the grey crosses represent the median estimated error for each of the parameters. Cells with only one galaxy are not coloured, instead we draw these individual galaxies as orange dots.

**Table C1.** Activity types found in the literature for unclassified and discrepant Seyfert galaxies.

Object ID	Activity classification types	References
No Type in VCV & SMB		
2MASX J12140343-1921428	Mixed blazar; QSO; Sy1	2,19; 16; 18
2MASX J23032790+1443491	Composite; Sy1	20; 18
CADIS 16-505716	QSO	18
LEDA 1485346	Sy1	18
LEDA 3095610	QSO; Sy1	16; 18
LEDA 3096762	QSO	18
MCG+00-11-002	Sy1	18
MCG+03-45-003	Sy1; Sy2	18; 23
QSO B1238+6232	QSO	18
[HB93] 0248+011A	QSO	18
Type in VCV or SMB		
2E 2294	QSO; Sy1	6,9,12,15,16,21; 18
2E 2628	QSO	6,9,13,15,16,18,21
2E 3786	QSO	6,9,13,15,16,18,21
2MASS J00423990+3017514	Sy1	18,23
2MASS J01341936+0146479	QSO; Sy1	6,16,18
2MASS J02500703+0025251	QSO; SF; Sy1	6,10,14,16,21,22; 8; 18,20
2MASS J08171856+5201477	Sy1; NLSy1	3,18,20; 7
2MASS J09393182+5449092	QSO; Sy1	16,9,4,18,21; 20
2MASS J09455439+4238399	QSO; Sy1; NLSy1	14; 20; 4,7,17,18
2MASS J09470326+4640425	QSO; NLSy1	6,9,16,18,21; 7
2MASS J09594856+5942505	QSO; Sy1	6,9,10,12,14,16,21; 18
2MASS J10102753+4132389	QSO	6,9,10,13,15,18,21
2MASS J10470514+5444060	QSO; Sy1	4,6,9,15,16,21; 18,20
2MASS J12002696+3317286	QSO; Sy1	16,9,6,14,21; 18
2MASS J15142051+4244453	QSO; Sy1	4,6,12,14,15,16,21; 18,20
2MASSI J0930176+470720	QSO; Sy1	6,9,23,16,18,21; 20
2MASX J02522087+0043307	QSO; Sy1; SF	4,14,16,22; 18,20; 8
2MASX J02593816+0042167	QSO; Sy1; SF	6,12,14,16,21,22; 18,20; 8
2MASX J06374318-7538458	Sy1	18
2MASX J09420770+0228053	Sy2; LINER	18; 20
2MASX J09443702-2633554	QSO; Sy1; Sy1.5	16; 18; 1
2MASX J09483841+4030436	QSO; Sy1	14; 18,20
2MASX J10155660-2002268	Sy1	18
2MASX J10194946+3322041	Sy1; NLSy1	18; 7
2MASX J15085291+6814074	Sy1	18
2MASX J16383091-2055246	Sy1; NLSy1	18; 1,5,11
2MASX J21033788-0455396	Sy1	18
2MASX J22024516-1304538	Sy1	18
2dFGRS TGN357Z241	QSO; Sy1	4,16; 18
3C 286	Mixed Blazar; QSO	2,19; 6,12,13,18,21
6dFGS gJ034205.4-370322	Mixed Blazar; QSO; Sy1	2,19; 16; 18
6dFGS gJ043944.9-454043	QSO	16,18
6dFGS gJ084628.7-121409	Sy1; NLSy1	18; 5
CTS 11	Sy1; NLSy1	18; 11
HE 0226-4110	QSO; NLSy1	16,18; 5
ICRF J025937.6+423549	Mixed Blazar; QSO	19; 18
ICRF J081100.6+571412	QSO	6,12,13,14,15,18,21
ICRF J100646.4-215920	Mixed Blazar; Sy1	2,19; 18
ICRF J110153.4+624150	BZQ; QSO; SF	2,18; 6,9,12,13,18,21; 8
ICRF J135704.4+191907	BZQ; QSO	2,18,23; 6,9,12,13,14,18,21
IRAS 10295-1831	Sy1	18
Mrk 1361	QSO; Sy1; Sy2	14; 20; 18
PB 162	QSO; Sy1; NLSy1; SF	14,16; 18,20; 7; 8
UGC 10683	Sy1	18

**References:** 1: Panessa et al. (2020); 2: D’Abrusco et al. (2019); 3: Liu et al. (2018); 4: Dong et al. (2018); 5: Chen et al. (2018); 6: Pâris et al. (2018); 7: Rakshit et al. (2017); 8: Duarte Puertas et al. (2017); 9: Gupta et al. (2016); 10: Ai et al. (2016); 11: Schmidt et al. (2016); 12: Albareti et al. (2015); 13: Gentile Fusillo et al. (2015); 14: Sun & Shen (2015); 15: Krawczyk et al. (2015); 16: Souchay et al. (2015); 17: Järvelä et al. (2015); 18: Flesch (2015), version 7.2 Flesch (2021); 19: D’Abrusco et al. (2014); 20: Toba et al. (2014); 21: Krawczyk et al. (2013); 22: Meusinger et al. (2011); 23: Cusumano et al. (2010), coordinates match within 2'', distance varies between 0.56'' and 1.77''.